



## *Lightweight Multifunctional Planetary Probe for Extreme Environment Exploration and Locomotion*

Final Report

*NASA Innovative Advanced Concepts (NIAC) Program Phase I*

Principle-Investigator: Javid Bayandor, Ph.D., CRASH Lab, Virginia Tech

Graduate Team Member: Kevin Schroeder, CRASH Lab Virginia Tech

Consultant: Jamshid Samareh, Ph.D, Vehicle Analysis Branch, NASA Langley Research Center



**Contents of Report**

**1. EXECUTIVE SUMMARY .....3**

**2. ORGANIZATION OF THE REPORT .....4**

**3. INTRODUCTION .....5**

**4. CONCEPT OVERVIEW .....6**

**5. EXTREME ENVIRONMENT COMPONENT DESIGN.....10**

**6. TANDEM SYSTEM ANALYSIS TOOL .....14**

**7. FREE FALL ANALYSIS.....19**

**8. IMPACT ANALYSIS.....25**

**9. CONTROL AND LOCOMOTION INVESTIGATION.....39**

**10. CONCEPTUAL MISSION TO VENUS.....43**

**11. CONCLUSION AND CONTINUING WORK .....49**

**12. ACKNOWLEDGEMENTS .....50**

**APPENDIX A: COMPARISON TO ADEPT .....51**

**APPENDIX B: COMPARISON TO VITAL .....53**

## **1. Executive Summary**

The demand to explore new worlds requires the development of advanced technologies that enable landed science on uncertain terrains or in hard to reach locations. As a result, contemporary Entry, Descent, Landing, (EDL) and additional locomotion (EDLL) profiles are becoming increasingly more complex, with the introduction of lifting/guided entries, hazard avoidance on descent, and a plethora of landing techniques including airbags and the sky crane maneuver. The inclusion of each of these subsystems into a mission profile is associated with a substantial mass penalty.

This report explores the new all-in-one entry vehicle concept, TANDEM, a new combined EDLL concept, and compares it to the current state of the art EDL systems. The explored system is lightweight and collapsible and provides the capacity for lifting/guided entry, guided descent, hazard avoidance, omnidirectional impact protection and surface locomotion without the aid of any additional subsystems.

This Phase I study explored:

1. The capabilities and feasibility of the TANDEM concept as an EDLL vehicle
2. Extensive impact analysis to ensure mission success in unfavorable landing conditions, and safe landing in Tessera regions
3. Development of a detailed design for a conceptual mission to Venus.

As a result of our work it was shown that:

1. TANDEM provides additional benefits over the Adaptive, Deployable Entry Placement Technology (ADEPT) including guided descent and surface locomotion, while reducing the mass by 38% compared to the ADEPT-VITaL mission<sup>1</sup>
2. Demonstrated that the design of tensegrity structures, and TANDEM specifically, grows linearly with an increase in velocity, which was previously unknown
3. Investigation of surface impact revealed a promising results that suggest a properly configured TANDEM vehicle can safely land and perform science in the Tessera regions, which was previously labeled by the Decadal Survey as, “largely inaccessible” despite its high scientific interest<sup>2</sup>.

This work has already resulted in a NASA TM and will be submitted to the Journal of Spacecraft and Rockets<sup>1</sup>.

## 2. Organization of the Report

The present report aims to provide an overview of the progress made, result found, and methodologies used in the Phase I of the awarded NIAC investigation. A thorough description of the TANDEM concept investigations is presented. It spans from the conception of TANDEM through its progress to an overall TRL of 2. The report is organized as follows:

Section 3 – Introduction of the fundamental technologies that enable the TANDEM concept

Section 4 – Overview of what the concept is, how it can be used, and what it enables in an EDLL sequence

Section 5 – A deconstruction of the components of TANDEM as well as a discussion of how high temperature components can be implanted into the current design and how they will benefit the concept

Section 6 – Overview and implementation of a developed 3-DOF flight mechanics code with incorporated modules for hypersonic aerodynamics, aerothermodynamics, and vehicle configuration control

Section 7 – Discussion of the development and implementation of a Computation Fluid Dynamics (CFD) simulation for the determination of terminal velocity and coefficient of drag

Section 8 – The development of impact modeling methodology and the discussion of a large parametric impact analysis to test omnidirectional protection

Section 9 – Description of three types of control strategies used and a discussion of the selected methodology for advance gait development

Section 10 – Overview of a detail design of a TANDEM vehicle for a conceptual mission to a Tessera Region on Venus

Section 11 – Summary of results found and on-going work

Section 12 - Acknowledgements

Appendix A – Comparison of the TANDEM concept to the Venera-class of landers, including a direct comparison to the VITaL and ADEPT-VITaL landers

Appendix B – Comparison of TANDEM to ADEPT

### **3. Introduction**

Tension Adjustable Network for Deploying Entry Membrane (TANDEM) is a hybrid of two innovative concepts under active research at NASA: tensegrity robotics and mechanically deployable semi-rigid heat shields. As payload sizes for robotic missions to other celestial bodies are growing larger, new entry vehicles are being explored that can handle greater payloads while still being able to fit within existing launch vehicles. Mechanically deployable heatshields open like an umbrella, allowing them to be stowed at a small cross sectional diameter and then deployed for entry to produce a large drag area. The most notable mechanically deployable heatshield is the well-established ADEPT concept<sup>3-7</sup>. ADEPT uses 3-D woven carbon fiber fabric as a flexible skin that functions as both the thermal protection system (TPS) and the structural support that transfers the aerodynamic loads to the frame of the entry vehicle. TANDEM uses the same fundamental concept as ADEPT but changes the deployment mechanism from spring-based compression to tensegrity-actuation. This provides the same benefits as ADEPT (low ballistic coefficient, lower entry g's, smaller launch vehicles, larger payloads, etc.) while seamlessly integrating the multifunctional tensegrity infrastructure.

Tensegrity systems provide a non-traditional solution to many problems encountered in a space mission. They distribute their loads through a network of tension cables while maintaining their shape through a set of discontinuous compression rods. The tension network is incapable of supporting a compressive load, thus the truss-like structure must be developed in a predetermined and stable geometry that confines the compressive loads to the compression members and the tensile loads to the tension network. By isolating the loads in this manner, the mechanical complexity of the structure is reduced. Furthermore, the truss-like structure utilized by tensegrity systems lend themselves to lightweight designs that make them extremely well suited to space related missions. By actuating the cables in the tension network, the outer shape of tensegrity structures can be drastically altered, allowing the system be stowed and deployed<sup>8-10</sup> or even controlled to produce a tensegrity robot<sup>11-13</sup>. The versatility of tensegrity provides TANDEM with its unique and multifunctional capabilities as discussed below. Figure 1 depicts TANDEM in a stowed (a) and deployed (b) configuration.

## TANDEM

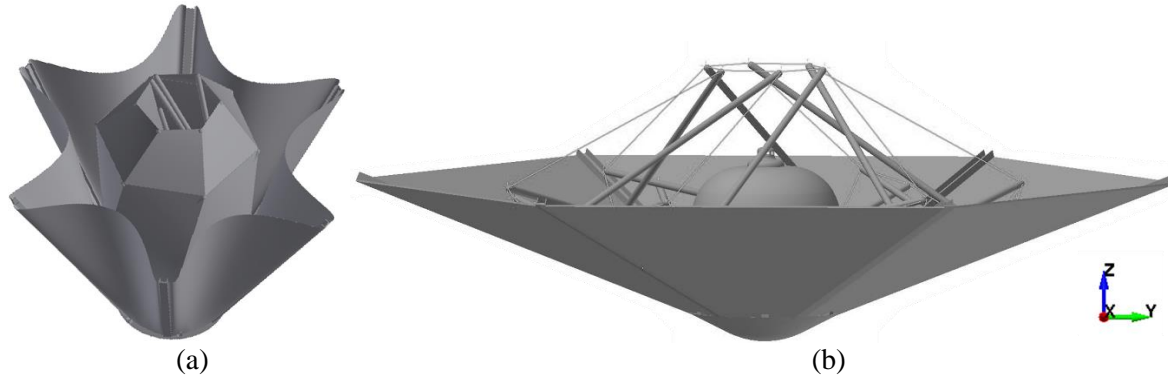


*Figure 1 The TANDEM Concept. (a) Stowed vehicle with heatshield and backshell. (b) Deployed vehicle with the carbon fabric of the back shell hidden*

Coupling tensegrity and ADEPT into a single design has significantly more advantages than either concept has separately. Tensegrity actuated deployable heat shields<sup>14,15</sup> have been proposed before, as have tensegrity lander/rovers<sup>13</sup>. But, to date, no one has presented a unified vehicle where one underlining tensegrity structure is capable of handling all of entry, decent, landing, and locomotion (EDLL). The systems level design approach to the EDLL sequence is what makes TANDEM unique. In most EDL (plus locomotion, if applicable) concepts, each leg of the sequence is handled by a separate system; the heatshield is unrelated to the landing mechanism and the payload (i.e., the rover) is typically considered dead mass until it has actually landed on the surface. In TANDEM, everything is connected to an actively controlled tensegrity frame so that the systems used for landing and locomotion are also utilized in entry and descent. TANDEM brings a new level of controllability to the EDLL sequence without increasing complexity or mass.

### 4. Concept Overview

TANDEM's lightweight and multifunctional design can be tailored to a variety of missions and is a feasible option for many atmospheric celestial bodies. Its mechanically deployable heat shield, high payload to structural mass ratio, and ability to safely impact the surface at high velocity makes TANDEM a great candidate for the next generation of robotic missions to Mars. Furthermore, its multifunctional capabilities during descent and omnidirectional protection on impact will be invaluable for landed missions to Titan or Venus where the thick atmosphere prevents the development of high resolution surface maps. Even on Earth, in inaccessible and hard to reach locations TANDEM is able to land nearby and roll to the desired location. In view of TANDEM's widespread applications, it was decided that in order to provide in-depth understanding of the concept, the breadth of the preliminary investigation should be focused on applications for a single planetary system. To this end, all of the subsequent work will be presented in the framework of a conceptual mission to the surface of Venus.

For launch and transit, the TANDEM vehicle will be stowed as shown in Fig. 1a. Upon arrival, TANDEM will detach from the cruise stage and deploys its heat shield. For simplicity, Fig. 2 visualizes the tensegrity structure and payload module, but the heatshield and backshell are attached to the tensegrity structure for deployment as shown in Fig. 1.

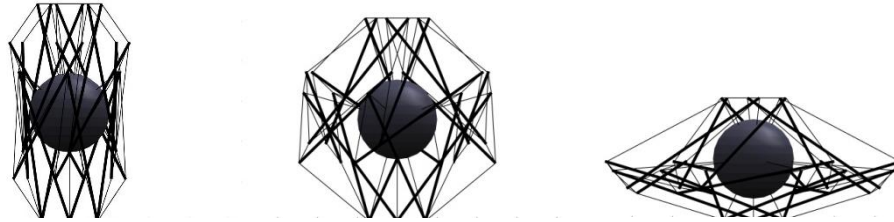


*Figure 2 Tensegrity structure changing configurations from stowed to deployed*

Traditional entries into the Venusian atmosphere typically had very steep flight path angles, ranging from approximately  $20^\circ$  to nearly  $80^\circ$ <sup>16</sup>. The flight path used was largely due to the characteristics of the TPS material, which had a high density and high thermal conductivity. In order to minimize the vehicle mass using such a material, high entry flight path angles (EFPA) were used to increase the magnitude of the peak heat pulse while its duration was shortened. Figure 3 shows the results of a parametric study where an entry vehicle with a nose radius of 1.125 m entering the Venusian atmosphere with a variety masses (i.e., ballistic coefficients) and flight path angles. As can be seen in the figure, the maximum entry load on the vehicle is almost exclusively dependent on the EFPA; the higher the angle, the higher the aerothermodynamic and g-loads. This is a limiting factor in type and amount of scientific payload that can be include in a mission to Venus. Much of the scientific equipment that is desirable for an in-situ mission to Venus is not capable of surviving the 200-400 g's experienced on entry with traditional entry vehicles. However, modern lightweight TPS concepts now exist that enable significantly shallower EFPA<sup>17,18</sup>. One method to achieve this is by using entry vehicles like TANDEM that leverage a low ballistic coefficient. The low ballistic coefficient of TANDEM enables it to enter at EFPA close to the skip out angle, reducing the expected entry loads to below well 100 g's. This expands the range of scientific equipment that can be included as well as reduces the expected mass of many instruments by 10% - 25% by reducing their required structural reinforcements<sup>3</sup>.

## TANDEM

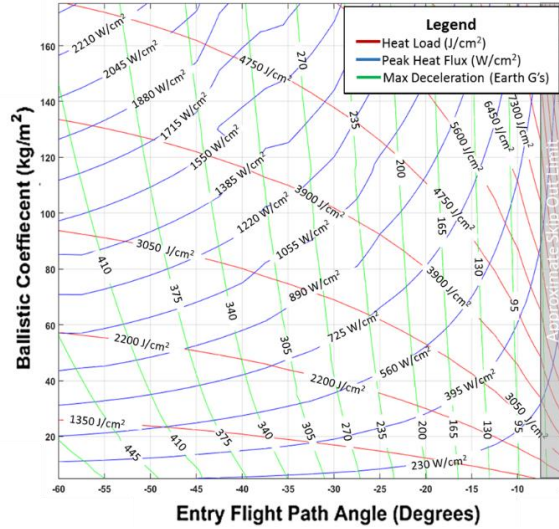


Figure 3 Ballistic coefficient parametric study as a function of entry flight path angle for ballistic entry at  $V_{entry}$  is 10.5 km/s and nose radius of 1.125 m

In addition to TANDEM's low ballistic coefficient, the vehicle has an efficient mechanism to provide lift. Mars Science Lab (MSL) is an example of entry vehicles using a lifting body. MSL achieved lift by using a total of 300 kg of ballast mass devices, ejecting the masses to shift the center of gravity of the vehicle. Alternatively, TANDEM is able to achieve lift with little to no mass penalty. The payload module is suspended by a number of cables design to actuate. This enables locomotion after landing, but can also be used to change the location of the payload module during entry, shifting the CG of the entry vehicle. With an offset CG, the vehicle will create a positive  $L/D$  ratio. Additionally, the payload can be shifted laterally in order to direct the lift vector and steep the vehicle. To ensure stability, the payload module will need to be kept low such that the vehicle's CG is below the aerodynamic center. The lifting entry allows the vehicle to decelerate in the upper atmosphere, maximizing the time spent on descent to collect more data samples than it could on a ballistic entry.

After entry, the TANDEM vehicle will eject the heat shield. The separation of the heat shield and TANDEM vehicle can be initiated by a spring-loaded mechanism. As the heatshield is ejected from TANDEM, it will no longer be able to maintain its deployed radius and will naturally return to a near-stowed, low cross sectional area configuration. There will be little chance of re-connect with the heatshield due to of the difference in ballistic coefficients (mass to drag ratio) of the heat shield and the descent stage of the TANDEM vehicle.

The descent stage may be equipped with parachutes to aid with the heat shield separation, but due to Venus's high density atmosphere, parachutes are not required to reach a safe landing velocity. Alternatively, the backshell can be used as a flexible drag device. Because the vehicle begins to heat up during the descent through the Venusian hot dense atmosphere, it can be advantageous to descend quickly to the surface to maximize the time spent there while still arriving at a safe velocity. This was achieved

previously in the Venera campaign by using a reefing cord to constrict part of the parachute. As the vehicle approached the surface, the atmospheric temperature increased, melting the reefing cord and allowing the parachute to fully open<sup>19</sup>. TANDEM is able to add to this concept by actively controlling its drag area. Utilizing the tension network, TANDEM can open and close its flexible backshell to control its rate of descent. This enables a balance between the need for a quick descent and the need of detailed exploration in various areas in the atmosphere that are of scientific interest. The Venus Exploration Analysis Group (VEXAG) has listed the atmospheric formation of Venus as the first goal for Venus exploration<sup>20</sup>. Unlocking the mysteries of the Venusian atmosphere will require a detailed investigation at key altitudes. A regulated descent can be used to maximize the vehicle's scientific investigation during the descent phase without excessively compromising its mission time on the surface. Based on a  $10.5 \text{ km/s}$  entry with a low EFPA and without the use of a parachute, it was found that the incorporation of the flexible backshell into an EDLL profile will create a range of descent times from as low as  $25 \text{ min}$  to as long as  $2 \text{ hrs}$ . Figure 4 shows the full range of descent trajectories that can be explored with TANDEM.

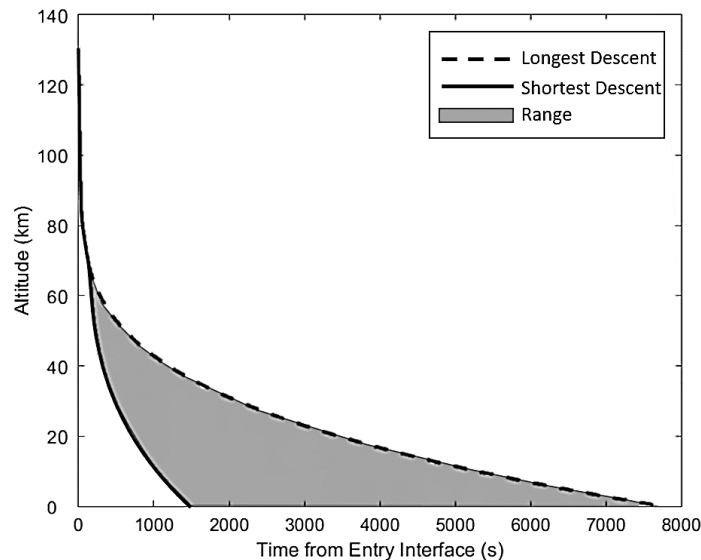


*Figure 4 Range of descent trajectories with the active control of the flexible drag plate*

When the vehicle is nearing its desired landing site, the flexible backshell can be adjusted to achieve pinpoint landing. The use of the backshell is analogous to how a parachutist can navigate to a specific landing site by pulling on cables to change the shape of the parachute. In the same way, controlling the shape of the flexible backshell can also be used as a simple form of hazard avoidance that can open up higher risk landing regions.

Once the vehicle is in the desired landing zone, the backshell can be released, allowing the rover to free fall to the surface. Depending on the ballistic coefficient for the specific mission, the terminal velocity for Venus applications could range from  $15$  to  $30 \text{ m/s}$ . Due to the large shock dissipating capability of

## TANDEM

tensegrity structures, TANDEM can be designed such that the landing overloads on the payload will be approximately the same  $g$ 's experience on entry. However, as the entry loads endure over time and the landing loads are only impulse loads, the onboard equipment will likely be able to handle a larger peak loading on impact compared to the peak loading experience on entry.

Like most spherical tensegrity concepts, TANDEM inherently provides omnidirectional protection on impact. Even if it impacts on a large boulder or a very uneven and sloped surface, TANDEM will survive with no complications. Omnidirectional impact protection opens up a host of landing sites (e.g., Venus's Tessera regions) that are too hazardous or too steep for traditional landers. Additionally, due to the unique shape altering capability of the TANDEM lander, the outer circumference of the vehicle can be actively adjusted while the payload module position can be altered to provide the optimal landing configuration for various landing scenarios. With its shock dissipating capability and omnidirectional protection, TANDEM provides a high level of reliability and safety to the mission.

As soon as the vehicle lands, it can begin traversing the surface. The tensegrity framework provides TANDEM with a more organic method of locomotion than a wheeled rover does. Tensegrity landers have a more diverse range of mobility, including rolling, sliding, bouncing, walking, and jumping, that cannot be safely performed by a traditional rover. These new modes of locomotion open up high-risk terrains for future missions. Additionally, previous missions have shown that being immobile presents a risk to the mission. The Venera 14 lander detached one of its lens caps directly under where the soil densitometer was designed to sample, thus significantly interfering with the experiment<sup>21</sup>. With TANDEM, these unexpected interferences can be avoided. While the investigation of all of these modes of transportation are outside the scope of this preliminary investigation, a proof of concept locomotion demonstration is provided in section **Error! Reference source not found.** as well as an investigation of advance gait development strategies for tensegrity structure.

### 5. Extreme Environment Component Design

The TANDEM vehicle can be broken into four basic components: The semi-rigid heat shield, the flexible backshell, the tensegrity structure, and the payload module. The following section provide a brief overview of these components. Many of the details mentioned in this section are mission dependent and can be altered based on the requirements and destination of each mission. A fuller discussion of the design process used for the conceptual mission developed in this study are discussed in Section **Error! Reference source not found.**

The semi-rigid heat shield, when fully deployed, is a 4.5 *m* diameter sphere-cone with a 70° degree cone angle. The nose of the shield is rigid and can be covered with a conventional TPS while the deployable components utilize a 3D woven carbon fabric. The carbon fabric has been arcjet tested based on the mission

requirements of the ADEPT-VITaL mission<sup>22</sup> up to  $250 \text{ W/cm}^2$ . The backshell is not exposed to the same aerodynamic and aerothermodynamic loads as the heat shield but it is still necessary to protect the aft of the vehicle during entry. As a result, there is a wider range of appropriate materials for its use. The nominal selection of backshell material for this analysis will be carbon fabric.

The tensegrity structure itself is comprised of 18 hollow titanium compression members and 78 individual titanium cables that comprise the tension network. Each rod in the structure has an ultra-high temperature and pressure motor<sup>23</sup> at either end which is used to spool in lengths of cable to control the configuration of the structure. In the center of the tensegrity structure is the payload module, an insulated pressure vessel used to protect the scientific equipment from the harsh environment. All of TANDEM's scientific equipment, control systems, and communications are housed inside of the payload module. This enables the uses of standard electronics for operation at Venus surface conditions (VSC). However, it also limits the lifespan of a mission. Because the payload houses so many mission critical systems, an ongoing work aims at increasing the operating temperature for several of the internal components. By reducing the number of components in the pressure vessel, the overall mass will significantly drop.

The implementation of an external pressure vessel as the central payload module was first utilized by the Soviet Union for the Venera missions<sup>24</sup> and is now common for new mission concepts<sup>25–28</sup>. However, housing these critical components inside of an external pressure vessel can be risky during landing or locomotion, in case the vessel strikes the ground. Additionally, in environments akin to VSC, this practice presents further risk to the mission by limiting the mission lifetime to the time required for the payload to reach its maximum operating temperature. In these conditions, the payload must endure not only the heat generated by its internal electronics, but also the extreme external temperatures. Equation 1, used to size the payload module, was derived from Zoelly's derivation of the critical external pressure required to prevent the buckling of a thin walled sphere. Zoelly's equation is a function of the material properties, radius, and thickness of the sphere<sup>29</sup>. An additional parameter was included to add a factor of safety to the pressure vessel.

$$t = \sqrt{F.S. \frac{Pr^2}{1.2E}} \quad (1)$$

As can be seen in Eq. 1, the thickness of the payload module is proportional to its radius. Thus, as the payload module increase in size, the mass of the pressure vessel increases cubically. Although it is largely unavoidable, the current practice of utilizing an insulated pressure vessel both limits the amount of equipment and increases the total system mass. By developing TANDEM's electrical and electromechanical components to operate in extreme environments, some of the internal components could be moved outside of the payload module. This would reduce the required size of the payload module for a

## TANDEM

TANDEM concept, thereby reducing mass; diversifying the locations of mission critical components; and extending mission life by decelerating the accumulation of thermal waste.

The current design of TANDEM utilizes standard electronics with a maximum operational temperature of 35°C. The thermal protection system (TPS) was considered to keep the payload module under that threshold for 3 hours after entry<sup>25</sup>. An ongoing investigation looks at the incorporation of high temperature electronics to enable the removal of components from the payload module. The rest of this section explores various components that can be designed to survive at VSC. The systems to be removed from the payload module can be fabricated using SiC based electronics, while components that must remain inside the payload module can be designed to operate at elevated temperatures by incorporating silicon on insulator (SOI) electronics. These are discussed herein in the order of their current high-temperature TRL and benefits for removal from the sealed payload module: motors and batteries, scientific instruments, and data storage and control system.

### **Motors and Batteries**

While an under-actuated TANDEM vehicle could be controlled from within the payload module, the batteries and motors produce significantly more heat than any of the other components, limiting the mission life. Additionally, creating a seal that allows the cable to be drawn through the wall of the pressure vessel presents a substantial design problem, especially at VSC. Therefore, batteries and motors are the most important components for which to develop a high temperature counterpart.

Fortunately, the required components exist at high TRLs. Honeybee Robotics has developed various stepper and brushless DC motors for extreme environments<sup>23</sup>. These motors have been tested over a large temperature range (20-460°C), so they are a feasible selection for TANDEM, which requires operation above the entry interface as well as on the surface. The required electronic motor controller will be addressed below under the Data Storage heading.

Batteries provide a more significant challenge. Landis provides a detailed overview of high-temperature battery systems that already exist<sup>30</sup>. The limiting factor with current technologies is that they require elevated temperatures before they become operational. Sodium-sulfur batteries, for example, only operate above the melting point of sulfur, 240°C<sup>30</sup>. This means that the power system would not start operating until after the vehicle descends below an altitude of at least 65 km.

Three potential solutions to provide an adequate power source are discussed and compared. Further investigation of these options will be addressed in future work. The first solution is to simply keep all of the batteries inside the payload module. This solution will act as the baseline case since it does not require any technology development. Keeping the batteries inside the payload is not preferred, as it results in a higher overall vehicle mass and increased thermal accumulation rate. Additionally, this method requires

electrical leads to be imbedded into each tension cable in order to transmit the power to each externally mounted motor.

The next alternative solution separates the power system required for the heat shield deployment from the additional system used for surface locomotion. This strategy may be partially required, due to the dichotomy of required torque for locomotion versus deployment. Because deployment of the heat shield also requires the entry membrane to be pretensioned, the high temperature motors may not be able to provide enough torque to deploy the heat shield. To resolve this, an additional motor has been included in the design of the aeroshell that has the sole purpose of assisting the pretensioning of the aeroshell. The proposed solution will allow the tensegrity motors to remain inactive and only utilize the aeroshell motor to transition from the stowed configuration to the deployed configuration. This method is still suboptimal, as it does not take advantage of the functionality of the vehicle; the multifunctional infrastructure will be inactive during entry and initial stages of descent. Yet, this solution will successfully remove the motors and batteries from the payload module, thus extending the mission timeline and potentially reducing the total mass of the system.

Finally, it may be possible to heat the battery before deployment. This is a common practice for thermal batteries, which have operational temperatures corresponding to VSC<sup>30</sup>. While thermal batteries will not be used in this mission due to their short service time, similar pyrotechnics may be used to initially heat up the batteries for operation during deployment and descent, and then the high atmospheric temperatures will keep the batteries at operating temperatures for locomotion. This solution provides the best characteristics but requires further investigation to confirm its feasibility.

### **Scientific Instruments**

The most sensitive components in the payload module are the scientific instruments. Although many of the instrument suites proposed for Venus landers are not designed to operate at VSC, NASA Glenn has developed a number of sensors and instruments that are functional at such conditions. Some of the developed high temperature sensors include pressure and temperature sensors, electric nose sensors (which can be doped to be sensitive to various chemical compounds), strain sensors (which could be used for feedback control of the vehicle), as well as Microscale Particulate Classifiers (MiPAC)<sup>31</sup>. Such instruments will be useful for characterizing the environment around the landing site, and will be used to answer the Decadal Survey's questions about Venus. Further investigation will be made into additional components that can be used for scientific exploration of Venus.

### **Data Storage, Avionic, and Control Systems**

Due to the high number of degrees of freedom, the control systems required for tensegrity robotics are highly complex. Despite this, Mirlletz et al. have produced an effective strategy for producing various

gaits through the use of a Neural Network, Central Pattern Generators (CPGs), and a machine learning algorithm<sup>11</sup>. Although the capability for control exists, the data storage required to hold an on-board library of various gait and control strategies may surpass the current state of the art for SiC components. For this reason, the on-board computer required to make calculations for each scenario in real time will have to remain inside the insulated payload module. Future work will investigate available SOI or similar systems that will raise the maximum operational temperature of the computational and data storage system. The nominal operational temperature of the current payload design is 35°C. However, standard electronics can be designed to operate as high as 60°C, but there is potential through military grade electronics to achieve operational temperatures as high as 125°C. Incorporation of any technique to raise operational temperature of internal components will significantly extend the mission lifetime compared to the baseline design.

Less complicated systems, such as the electronic motor controller, can be designed to operate at VSC. In fact, an electronic controller has already been developed for the Honeybee motor. An additional inclusion of a short range Radio Frequency (RF) transmitter/receiver capable of operating at VSC will enable wireless communication from the on-board computer to the motor controllers, thus removing any feedthroughs in the pressure vessel wall.

## **6. TANDEM System Analysis Tool**

A system analysis tool was developed to aid in the design of a mission utilizing the TANDEM concept. This tool analyzes key parameters of the vehicle during its EDLL sequence. The analysis tool uses a 3-DOF flight mechanics code as its backbone with additional modules integrated into it. Throughout the various stages, a tensegrity form finding algorithm is used to solve for the static configuration of the vehicle. During the entry stage, the tool investigates the aerodynamics and aerothermodynamics using the modified Newtonian method and surrogate convection and radiation models, respectively. Because all of these methods are low computational-expense approaches, a large number of different entry and descent sequences can be analyzed rapidly. Landing and locomotion were analyzed by integrating outside codes into the analysis tool. Time explicit finite element models with user defined algorithms were used on the LS-Dyna platform for impact simulations, and the NASA Tensegrity Robotics Toolbox (NTRT) was implemented for locomotion analysis and control. An overview of the system analysis tool is provided in Fig. 5 while additional information on each of the modules is provided in the following sections.

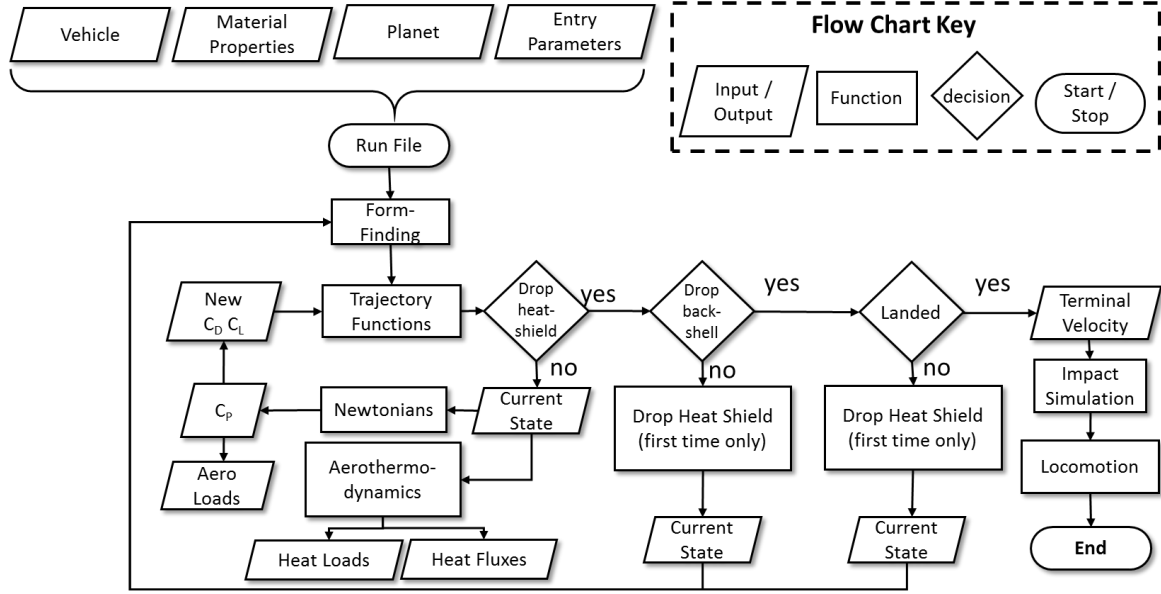


Figure 5 TANDEM System Analysis Tool flowchart

### A. Flight Mechanics

A 3-DOF flight mechanics code (FMC) was developed to calculate the trajectories used during the proposed mission. The FMC used the Runge-Kutta method with a 5<sup>th</sup> order accuracy using Matlab's ODE45 function<sup>32</sup> to integrate the following system of ordinary differential equations (ODEs). Together, these equations define the position, velocity, and orientation of the vehicle throughout its atmospheric entry and descent phases.

$$\begin{aligned} \frac{dv}{dt} &= -\frac{D}{m} - g \sin(\phi) & V \frac{d\phi}{dt} &= \frac{L}{m} - \left(g - \frac{mV^2}{R_v}\right) \cos(\phi) \\ \frac{ds}{dt} &= \frac{R_p}{R_v} V \cos(\phi) & \frac{dR_v}{dt} &= V \sin(\phi) \end{aligned} \quad (2)$$

### B. Aerodynamics

The aerodynamic loads and aerothermodynamics are determined from the state parameters defined after each time step of the Runge-Kutta integration. The aerodynamic loads are estimated using the modified Newtonian method, which uses the Mach number, atmospheric specific heat ratio, and the vehicle geometry to estimate the coefficients of pressure, lift, and drag. During the hypervelocity entry phase, the coefficients are updated at each time step. The modified Newtonian method approximates the flow over the vehicle as a purely inviscid stream of particles. This assumption reduces the calculation of the aerodynamic loads to a simple algebraic equation. This method has been shown to provide accurate approximations for hypersonic and supersonic speeds<sup>33</sup>. A complete derivation of Eq. 3 has been carried out by Anderson<sup>34</sup>

$$C_p = C_{p_{max}} \sin^2 \theta \quad (3)$$

where the coefficient of pressure at the stagnation point can be analytically derived as a function of Mach number and specific heat coefficient as seen in Eq. 4

Table 1 Atmospheric Density as a Function of Altitude

Altitude (km)	Atmospheric density, $\rho$ (kg/m <sup>3</sup> )	Speed of Sound, (m/s)
0	64.80	427.6
10	37.70	402.0
20	20.40	376.9
30	10.20	348.4
40	4.400	319.7
50	1.590	293.3
60	0.469	254.1
70	8.390x10 <sup>-2</sup>	237.8
80	1.190x10 <sup>-2</sup>	220.3
90	1.150x10 <sup>-3</sup>	204.3
100	7.990x10 <sup>-5</sup>	207.2
110	5.810x10 <sup>-6</sup>	197.1
120	3.200x10 <sup>-7</sup>	199.2
130	1.850x10 <sup>-8</sup>	209.1
140	1.390x10 <sup>-9</sup>	233.9
150	1.610x10 <sup>-10</sup>	276.0

$$C_{P_{max}} = \frac{2}{\gamma M^2} \left[ \left( \frac{M^2(\gamma+1)^2}{4\gamma M^2 - 2(\gamma-1)} \right)^{\frac{\gamma}{\gamma-1}} \left( \frac{1-\gamma+2\gamma M^2}{\gamma+1} \right) - 1 \right] \quad (4)$$

where  $\gamma$  is 1.3 for Venus atmosphere. With the  $C_p$  of the current time step known, the pressure and aerodynamic load on the vehicle can be solved at any point in the exposed flow field using Eq. 5.

$$p - p_\infty = \frac{1}{2} C_p \rho_\infty V_\infty^2 \quad (5)$$

The drag and lift are simply the normal and tangential components of the total aerodynamic load, respectfully. From that, the  $C_D$  and  $C_L$  of the current time step can be calculated using Eqs. 6 and 7. The updated lift and drag coefficients are then applied to the trajectory equations (Eq. 2) for each time step.

$$C_D = \frac{D}{2S\rho_\infty V_\infty^2} \quad (6)$$

$$C_L = \frac{L}{2S\rho_\infty V_\infty^2} \quad (7)$$

The free stream velocity,  $V_\infty$ , is a state variable and the atmospheric density,  $\rho_\infty$ , is found as a function of altitude. A simple atmospheric model seen in Table 1 from Braun and Justus<sup>35</sup> are used for these calculations.

### C. Aerothermodynamics

The aerothermodynamics are a nontrivial value to calculate. Thus, surrogate equations are used to estimate the convective and radiative heat flux experienced by the vehicle during atmospheric entry. These equations provide the stagnation-point heat fluxes for an axisymmetric blunt body in arbitrary gases at chemical equilibrium. The surrogate equations are tuned to match empirical data or values predicted by higher fidelity models, as functions of only the vehicle's velocity, nose radius, and the atmospheric density.

$$Q = KV_\infty^a \rho_\infty^b R_n^c \quad (8)$$

The constants  $K$ ,  $a$ ,  $b$ , and  $c$  are selected to match different entry conditions and vehicle parameters. Multiple surrogate equation constants, shown in Table 2 for convection heating and Table 3 for radiation heating, were reviewed for this step of the analysis to ensure that the results were reasonable and conservative.

Table 2 Convective Heating Surrogate Equation Constants

Author	K	a	b	c
Sutton and Graves <sup>36</sup>	1.896x10 <sup>-4</sup>	3	0.5	-0.5
Scott et al. <sup>37</sup>	1.1547x10 <sup>-4</sup>	3.05	0.5	-0.5
Tauber, Bowles, and Yang <sup>38</sup>	1.35x10 <sup>-4</sup>	3.04	0.5	-0.5

Table 3 Radiation Heating Surrogate Equation Constants

Author	Range	$K$	$a$	$b$	$c$
Park and Ahn** <sup>39</sup>	All	$2.787 \times 10^{-67}$	19	1.05	0.2
	$12 \text{ km/s} > V_\infty > 10 \text{ km/s}$	$3.07 \times 10^{-44}$	13.4	1.2	0.49
Craig and Lyne <sup>40</sup>	$10 \text{ km/s} > V_\infty > 8 \text{ km/s}$	$1.22 \times 10^{-12}$	5.5	1.2	0.49
	$V_\infty < 8 \text{ km/s}$	$3.33 \times 10^{-30}$	10	1.2	0.49
Tauber, Palmer, and Prabhu <sup>41</sup>	$12 \text{ km/s} > V_\infty > 10 \text{ km/s}$	$8.497 \times 10^{-63}$	18	1.2	0.49
	$V_\infty < 10 \text{ km/s}$	$2.195 \times 10^{-22}$	7.9	1.2	0.49

\*\*NOTE: The normalized pyrolysis-gas injection rate was assumed to be 0 to provide the most conservative approximation

There was very little variation between the various convection models, however, Sutton and Graves’s model was selected for the convection calculation. Sutton and Graves’s model is unique in its capability to be used for various atmospheric bodies<sup>36</sup>. The constant  $K$  in their model was derived from the constituents of the atmosphere and is predefined for various atmospheric bodies in the solar system. The ability to develop a new heating constant for an arbitrary gas will be utilized further in future work, which will analyze the merit of TANDEM on other planetary bodies. Meanwhile, the radiation calculation constants were selected to be the Tauber, Palmer, and Prabhu model because its assumptions match better than the Craig and Lyne model, and the total heat load was more conservative than the Park and Ahn model. Figure 6 shows the convective and radiative heat fluxes at the stagnation point during entry.

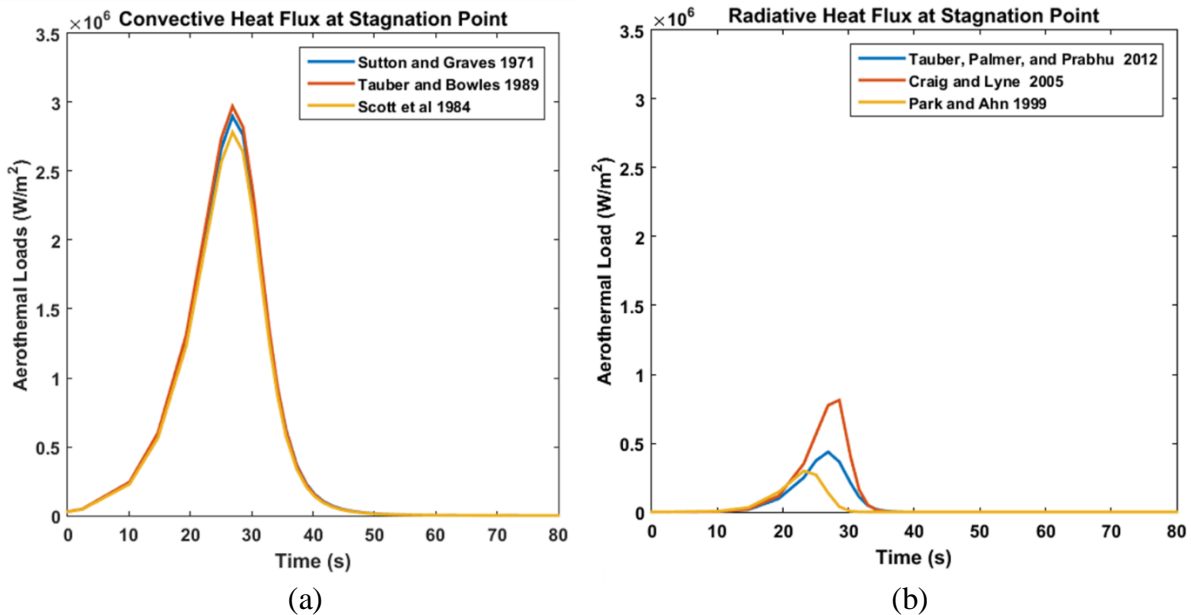


Figure 6 Comparison of various aerothermodynamic surrogate models for (a) convective heat flux and (b) radiative heat flux

After a threshold altitude or acceleration value is reached, the heat shield is released. This transition is approximated by a  $C^1$  discontinuity in the trajectory calculations (i.e. a discontinuity in the derivative of

the position function). The vehicle's mass and ballistic coefficient are changed as the heat shield is released. This reflects the descent stage of the EDL sequence where the vehicle is decelerated by the flexible backshell or parachute. In this stage, the Newtonian method is no longer applicable and thus a user defined  $C_D$  and  $C_L$  must be supplied. An additional  $C^1$  discontinuity can be included to capture the release of the backshell before landing in order to calculate the terminal velocity of the vehicle.

#### D. Form-Finding Algorithm

When the vehicle reaches an altitude of zero, the flight mechanics code stops and the final velocity of the vehicle is recorded for use in the landing simulation. The landing simulation utilizes an explicit finite element code to simulate the vehicle impacting on a rigid surface. Because the stiffness of a tensegrity structure is closely dependent on its configuration, it is necessary to use a form-finding algorithm before creating the finite element (FE) model to ensure that the structure is in a stable configuration. If there is too much slack in the tension network, the structure will be unable to hold a load. Form-finding algorithms can utilize a variety of numerical methods to find a stable 3-D configuration for the tensegrity structure. Tibert and Pellegrino's survey of various methodologies presents a good overview of the most prominent form-finding algorithms<sup>42</sup>. For this study, the nonlinear constrained optimization method presented by Pellegrino<sup>43</sup> was selected, because it provided the most controllability for various configurations. This method uses nonlinear constrained optimization to maximize the length of the compression members for a given tension network. This, in turn, removes any slack in the structure, creating a stable configuration (i.e., a configuration where the cables are all in tension and the rods are in compression).

Given the connectivity matrix of the structure and the normalized lengths of the outer cables in the tension network, the nodal coordinates are determined such that Eq. 9 is maximized.

$$\begin{aligned} & \text{maximize} && l_c^2 \\ & \text{Subject to} && \begin{cases} l_{T_1} - l_{T_1} = 0 \\ l_{T_2} - l_{T_2} = 0 \\ \vdots \\ l_{T_{n-1}} - l_{T_{n-1}} = 0 \\ l_{T_n} - l_{T_n} = 0 \end{cases} \end{aligned} \quad (9)$$

where  $l_c$  and  $l_{T_i}$  are the normalized lengths of the compression and tension members respectively, and are functions of their end point positions. After the optimization, the newly configured structure was scaled to the appropriate size for the mission. The code was developed so the TANDEM vehicles for various missions and mission requirements could be developed. Figure 7 shows the output of the form-finding algorithm for two different models with a different number of rotation sections.

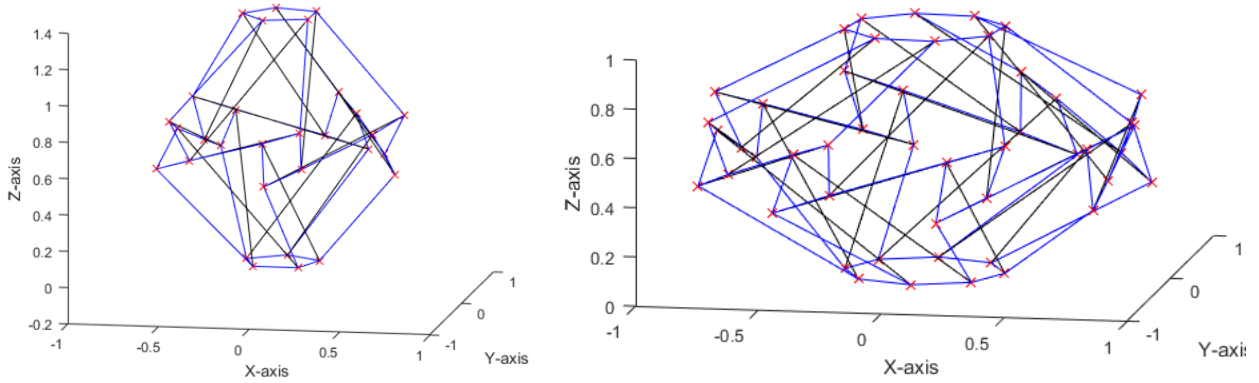


Figure 7 Various results from the form-find algorithm for a model (a) with 5 rotational sections (b) with 8 rotational sections

Table 4 reports the normalized lengths of each tension member for four vehicle configurations of the baseline design which has 6 rotational sections. The results of this algorithm are then used in developing the FE model for impact analysis. The method can also be used to develop the required control strategies for configuration transitions throughout the EDLL sequence as discussed in Section **Error! Reference source not found.**

Table 4 Form-Finding Input Parameters of Standard Configurations

Configuration	Normalized Length of Each Tension Member								
	Member 1	Member 2	Member 3	Member 4	Member 5	Member 6	Member 7	Member 8	Member 9
Stowed	2.40	3.50	1.50	1.50	3.50	2.40	1.00	3.00	1.00
Deployed	2.85	1.00	1.00	1.00	1.00	4.00	1.00	3.00	1.00
Descent	4.00	1.00	1.00	1.00	1.00	2.85	1.00	3.00	1.00
Landing	1.50	1.00	1.00	1.00	1.00	1.50	1.00	1.25	1.00

## 7. Free Fall Analysis

In order to find an accurate  $C_D$  to be used in systems analysis tool, the low-altitude portion of the atmospheric descent was investigated using CFD. The free falling TANDEM vehicle was analyzed parametrically by varying both fall speed ( $V_\infty$ ) and rotational velocity ( $\omega$ ) independently to understand how those parameters affect the drag to weight balance and determine a more accurate terminal velocity/landing condition. The analysis assumed that  $D/W = f(V_\infty, \omega)$ , and that rotational acceleration ( $\alpha_z$ ) was also equal to some function  $f(V_\infty, \omega)$ . The true landing scenario was one in which  $D/W = 1$  and  $\alpha_z = 0$ .

## TANDEM

The fluid domain consisted of a cylinder with a radius of 15 m and a height of 50 m, with an inlet located in the  $-Z$  direction and an outlet at  $+Z$ . TANDEM was located 10 m from the inlet on cylinder axis. The cylinder wall was modeled as having a velocity equal to the velocity defined at the inlet. The vehicle location, shown in yellow, and fluid domain is represented two-dimensionally in Fig. 8 and in three-dimensions in Fig. 9.

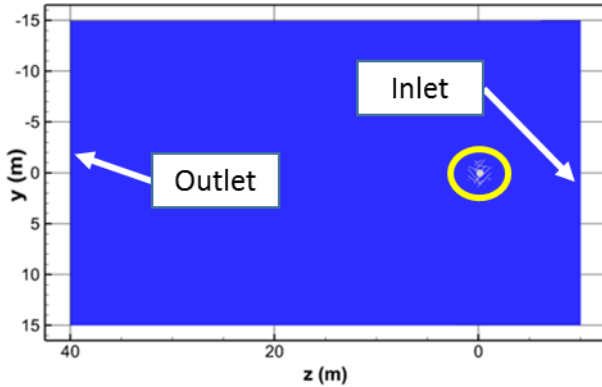


Figure 8 Cross-sectional slice of the fluid domain, highlighting the inlet, outlet, and TANDEM lander module.

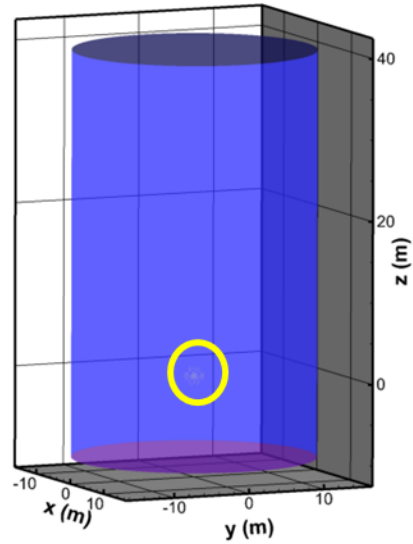


Figure 9 Full three-dimensional domain used in simulations, highlighting the size of the domain relative to the lander.

The fluid was modeled as carbon dioxide with fluid properties at VSC: density ( $\rho$ )  $64.8 \text{ kg/m}^3$ , and a dynamic viscosity ( $\mu$ ) of  $3.12 \times 10^{-5} \text{ kg/m} \cdot \text{s}$ <sup>44,45</sup>. The cables of TANDEM were assumed to be negligible. Neglecting the cables yielded a more conservative estimate for terminal fall speed and significantly improved computational time.

Two groups of cases were employed to better understand the expected landing scenario. The first set of cases involved TANDEM falling without rotating to develop an initial estimate of terminal velocity. Once an approximate terminal velocity was established, defined rotational velocities were applied to the system. The rotational velocity was modeled using a moving reference frame, with the inlets and outlets defined relative to the reference frame. The TANDEM lander was modeled as being stationary with regards to the absolute reference frame, allowing the fluid to rotate around the lander.

The commercial software ANSYS Fluent (v.17) was used to resolve the fluid domain around the vehicle during the free fall stage just before landing. The unsteady, incompressible Navier-Stokes equations were employed with a Shear-Stress Transport (SST)  $k-\omega$  turbulence model to accurately resolve the flow field. The continuity equation is shown in Eq. 10:

$$\nabla \cdot \vec{v} = 0 \quad (10)$$

Where  $\vec{v}$  is the velocity vector. Neglecting gravitational effects, the momentum equations are shown in Eq. 11:

$$\rho \left[ \frac{\partial \vec{v}}{\partial t} + \vec{v} \cdot \nabla(\vec{v}) \right] = -\nabla P + \nabla \cdot \bar{\tau} \quad (11)$$

where  $t$  is time,  $P$  is pressure, and  $\bar{\tau}$  is the fluid stress tensor.

The transient, incompressible continuity and momentum equations were solved using the segregated pressure-based Navier-Stokes (PBNS) solver in conjunction with the Semi-Implicit Method for Pressure Linked Equations (SIMPLE) algorithm<sup>46</sup>. The SIMPLE algorithm resolves the pressure-velocity coupling by enforcing mass conservation using a correction factor between element pressure and fluid flux. The gradients were discretized using the Least Squares Cell Based (LSCB) method. Pressure was discretized using the Pressure Staggering Option (PRESTO!) scheme, which utilizes a discrete continuity balance for a control volume about an element face to compute the pressure at that face. Momentum, Turbulence Kinetic Energy, and Specific Dissipation Rate were all solved using the Quadratic Upstream Interpolation for Convective Kinematics (QUICK) scheme. The QUICK method uses a weighted average of second-order-upwind and central interpolations of the variables with a variable, solution-dependent weight chosen to avoid introducing solution extrema, yielding a third-order accurate solution. Solution time was discretized using a bounded second-order implicit scheme.

The SST  $k$ - $\omega$  turbulence model used the empirical transport equations, Eq 12 and Eq 13:

$$\frac{\partial}{\partial t}(\rho k) + \frac{\partial}{\partial x_i}(\rho k u_i) = \frac{\partial}{\partial x_i} \left( \Gamma_k \frac{\partial k}{\partial x_j} \right) + G_k - Y_k + S_k \quad (12)$$

And

$$\frac{\partial}{\partial t}(\rho \omega) + \frac{\partial}{\partial x_i}(\rho \omega u_i) = \frac{\partial}{\partial x_i} \left( \Gamma_\omega \frac{\partial \omega}{\partial x_j} \right) + G_\omega - Y_\omega + S_\omega \quad (13)$$

where  $k$  is the turbulence kinetic energy,  $\omega$  is the specific dissipation rate,  $G_k$  represents turbulence energy generation due to mean velocity gradients,  $G_\omega$  represents the generation of  $\omega$ . The effective diffusivities of  $k$  and  $\omega$  are  $\Gamma_k$  and  $\Gamma_\omega$ , respectively.  $Y_k$  and  $Y_\omega$  are the dissipation of  $k$  and  $\omega$  due to turbulence. The SST model was specifically calibrated to accurately compute flow separation from smooth surfaces, which are widely used in modeling aerodynamic flows<sup>47</sup>. A convergence criterion of  $1 \times 10^{-5}$  is used for all residuals.

Each simulation was initialized and ran as steady-state for 200 iterations before switching to the transient solution. While the actual solution of the problem was inherently transient, the initial steady-state

solution reduced the overall time required before the solution reached the final value. The final reported solution for each velocity case, translational or rotational, was averaged over 0.2s.

In Fig. 10, the instantaneous flow fields for the rotating (right) and non-rotating (left) cases are compared using iso-surfaces and streamlines. Forcing the lander to remain static during entry, causes a very small, well-defined wake region behind the TANDEM lander with roughly straight streamlines after a short distance behind the lander. Allowing rotation significantly increased the overall size and complexity of the wake region, with large, clear vortex structures trailing well behind the vehicle.

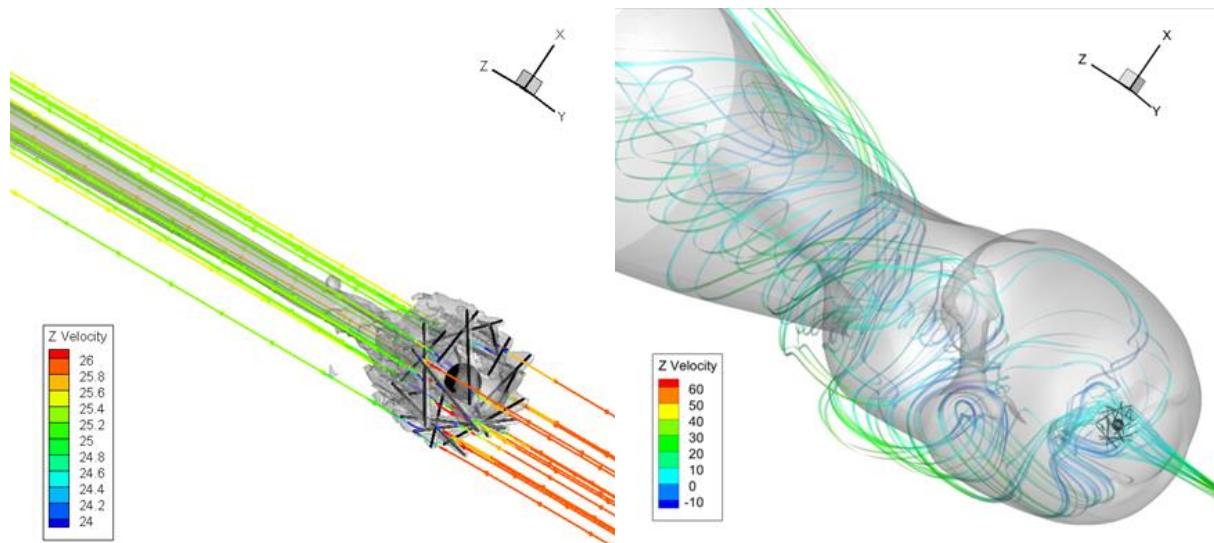


Figure 10. Juxtaposition of the non-rotating (left) 26 m/s entry and entry with a defined 5 rad/s rotation (right); with iso-surfaces defined at a z-velocity of 25 m/s at left and 8 m/s at right

Parametrically studying the entry envelope allowed the creation of analytical equations to describe, approximately, the relationship between drag force and flight velocity, as well as between Z-axis moment and rotational velocity.

### Non-Rotating Entry

Three non-rotating entry cases were evaluated to determine the relationship between velocity, drag force and rotational moment. The only variation between each of the three simulation cases was flight velocity, which was held at values of 10, 20 and 26 m/s. The drag force contribution by the compression members and payload are shown in Table 5 for velocities of 10, 20, and 26 m/s. The drag force contribution associated with the compression members is roughly seven times that of the payload across all velocities. The disparity in drag force between the compression members and payload is due, in part, to the compression members entraining flow in the space between the members and payload. The entrainment reduces the effective velocity experienced by the payload, contributing to a decreased drag force.

The Z-moment for the payload and compression members, shown in Table 5, was entirely caused by the angle of the compression members relative to the incoming flow. The relative angle and rotational symmetry of the compression members caused a significant moment force while the moment due to the payload was minimal due to its axisymmetry.

Table 5 Drag force and Z-Moment breakdown for the compression members and payload at 10, 20, and 26 m/s.

$V_\infty$ (m/s)	Payload		Compression Member	
	$F_D$ (N)	$M_Z$ (N-m)	$F_D$ (N)	$M_Z$ (N-m)
10	132.3	-0.1905	967.8	-177.1
20	572.7	-0.5739	3826.6	-689.9
26	955.4	-1.2302	6443.2	-1164.5

Time averaging the drag force and moment, and dividing by the predicted mass from section 10 and the predicted moment of inertia ( $405.7 \text{ kg m}^2$ ), respectively, yields the  $D/W$  ratio and rotational acceleration ( $\alpha_z$ ) of the system. The resulting  $D/W$  and  $\alpha_z$  are shown in Fig. 11. Analyzing Fig. 11, there are approximately second-order relationships for both  $D/W$  and  $\alpha_z$ :

$$(D/W)_v = 0.0014V_\infty + 0.0008V_\infty \quad (14)$$

and

$$\alpha_{z,v} = -0.0042V_\infty - 0.0021V_\infty \quad (15)$$

where Eq. 14 coincides with a ballistic coefficient of  $2,456 \text{ kg/m}^2$ , or a  $C_D$  of roughly 0.006 based on a circular frontal area with a radius equal to that of the TANDEM model. Based on the predicted mass of the lander and the analytical model relating translational velocity to  $D/W$ , a terminal velocity of roughly  $26.5 \text{ m/s}$  is expected.

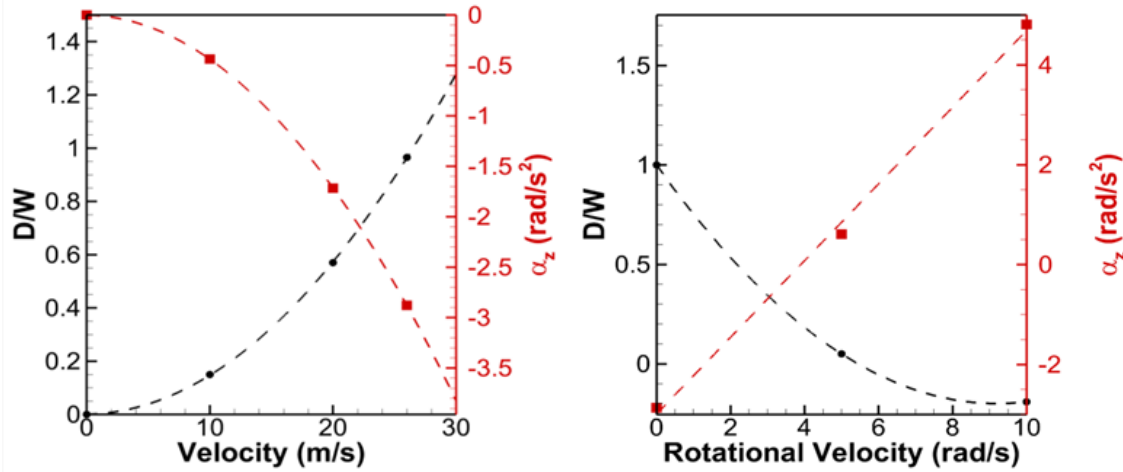


Figure 11 Drag to Weight ratio ( $D/W$ ) for the TANDEM lander versus inlet velocity for the translational (left) and rotational (right) velocity cases. Black circles represent  $D/W$  and red squares show the angular acceleration around the fall-axis. Dashed lines show the results of second-order polynomial fit lines for both curves for the translational cases and the  $D/W$  for rotational. A linear fit is used for the angular acceleration of the rotational case.

### Rotating Entry

Three cases were used to develop an analytical model to relate  $D/W$  and  $\alpha_z$  with the rotational velocity of the TANDEM lander. All cases considered a translational velocity of  $26 \text{ m/s}$ , due to being near the non-rotational terminal velocity. Rotational velocities of  $-5 \text{ rad/s}$  and  $-10 \text{ rad/s}$  were chosen for the rotational cases, with the third data point used from the  $26 \text{ m/s}$  non-rotating case.

The time-averaged results of the rotating cases are shown in Fig. 11, comparing  $D/W$  and  $\alpha_z$  with the rotational velocity of the lander. Similar to what was shown in the non-rotating entry simulations, a second-order relationship between rotational velocity ( $\omega$ ) and  $D/W$  was found:

$$D/W = 0.0142\omega^2 + 0.0261\omega + (D/W)_v \quad (16)$$

where  $(D/W)_v$  is the drag to weight ratio for the non-rotating case. A second, linear relationship is found for  $\alpha_z$  and  $\omega$ :

$$\alpha_z = -0.768\omega + \alpha_{z,v} \quad (17)$$

where  $\alpha_{z,v}$  is the angular acceleration from the non-rotating cases. Combining Eq. 16 with Eq. 14, and Eq.19 with Eq. 17, we find the approximate relationship for  $D/W$  and  $\alpha_z$  as a function of both  $\omega$  and  $V_\infty$ :

$$\frac{D}{W} = 0.0142\omega^2 + 0.0261\omega + 0.0014V_\infty^2 + 0.0008V_\infty \quad (18)$$

and

$$\alpha_z = -0.768\omega - 0.0042V_\infty^2 - 0.0021V_\infty \quad (19)$$

The results of Eqs. 18 and 19 are shown on the left and right sides of Fig. 12, respectively. Looking first at the left plot in Fig. 12, it is clear that as rotational velocity decreases for a given translational velocity,  $D/W$  increases. Conversely, for a given rotational velocity as translational velocity increases, so as  $D/W$ . Considering that the terminal translational velocity for an object is where  $D/W = 1$ , there is a line where the terminal translational velocity might lie. Bringing the right side of Fig. 12 into this context, we can see that the lines for  $D/W = 1$  and  $\alpha_z = 0$  overlap, which continue for a wide range of masses. Based on Eqs. 18 and 19, the true terminal velocity of the lander therefore should be around  $25.2 \text{ m/s}$  with a rotational velocity of  $-3.53 \text{ rad/s}$ .

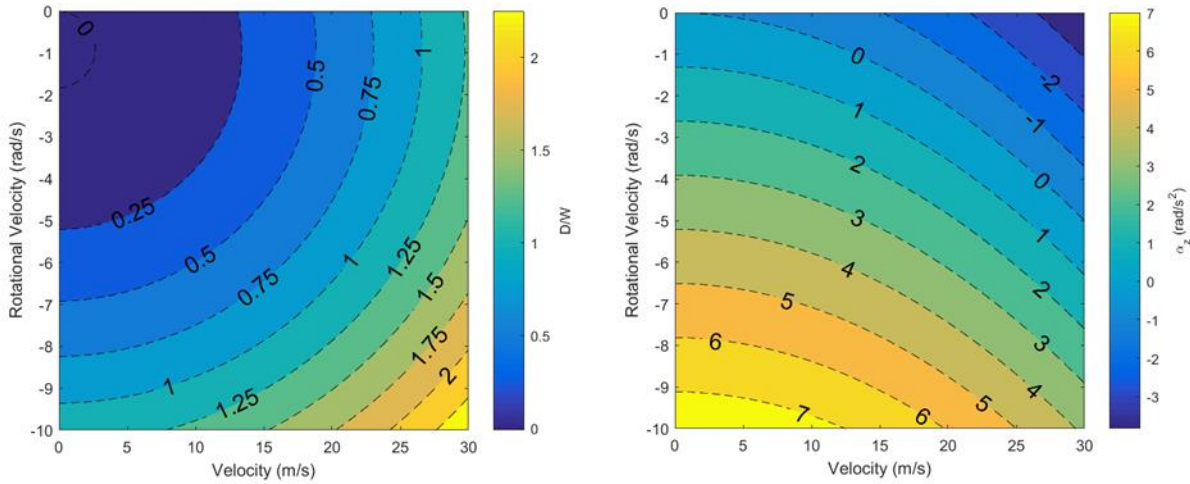


Figure 12. (left) A contour plot showing how  $D/W$  changes with respect to both rotational and translational velocity, with the terminal velocity being possible at any point along the 1 contour level. (right) A contour plot showing how  $\alpha_z$  changes with both rotational and translational velocity, the terminal rotational velocity lies anywhere along the 0 contour level.

## 8. Impact Analysis

As part of the investigations, it was attempted to show that TANDEM was able to provide sufficient impact resistance to enable safe landing in the Tessera region. A methodology was developed to accurately and efficiently predict the structural response of TANDEM during impact. In the development of this methodology a variety of explicit finite element models of various complexity were developed.

In order to maintain a low computational expense, it is preferable to model the tensegrity structure using only beam or rod elements. As the primary loads acting on the tensegrity structure are in line with each component, a 1-D element appears to be a reasonable modeling assumption. In order to verify this modeling assumption, a comparison of element formulations was conducted to show if vehicle response was preserved throughout the various modeling methodologies. Figure 13 shows a comparison of the TANDEM model with the compression members designed with 1-D beam elements and 2-D shell elements. Both models are identical except the type of element used to model the compression members. For this study all of the tension members were modeled with a 1-D cable element. The cable element utilized a bilinear, elastic constitutive relation; under a tensile loading the cable was perfectly elastic, whereas when the element was placed in compression, the cable provided no resistance.

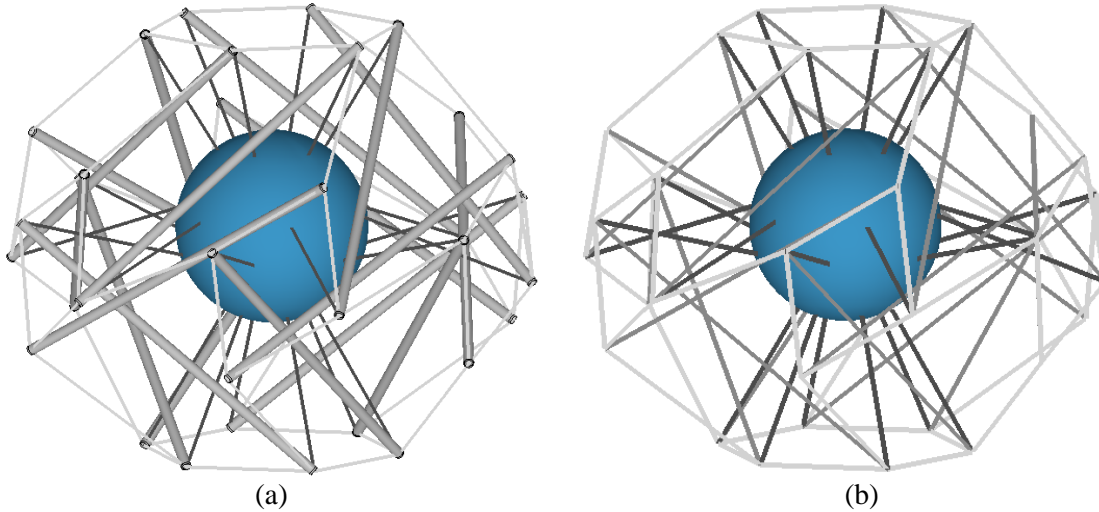


Figure 13 Identical finite element models of TANDEM using two differing modeling methodologies. (a) shell element formulation (b) beam element formulation

Four models were developed for each compression member element formulation type. Two models used rigid elements for the compression members with the other two using deformable elements. The other parameter explored was whether or not a mesh refinement should be used in modeling the tension members. For purely axial loading, with no dynamic effects, a single 1-D element can fully capture the deformation of a rod or beam. However, the dynamics of the impact scenario induced a non-axial inertial load on the tension members. A mesh refinement of the cable elements allows them to deform in a transverse direction based on these inertial loads.

In designing a tensegrity structure for impact speeds ranging from 15  $m/s$  to 30  $m/s$ , it is important to have well-designed compressive members. If they are under-designed, the compressive members may buckle on impact. Fortunately, member buckling (even multi-member yielding) does not always result in mission failure, as the load will be redistributed throughout the tension network. If the compression members are significantly over designed, the resulting structure will be too heavy to be supported. An over designed structure can lead to tension member failure, excessive shock response, and can also result in the payload module impacting the surface. Additionally, it is also important not to put the tensegrity frame in its stiffest configuration. An overly-stiff configuration will result in excessively large g-loading. However, if the lander configuration is too compliant, the payload module may contact some of the compressive members or the surface on impact. Both of these contacts can lead to mission failure, as they can cause the pressure vessel to buckle, damaging the scientific equipment inside. All of these considerations must be taken into account during the impact analysis stage in order to produce a viable tensegrity lander.

Utilizing the vehicle terminal velocity from the flight mechanics simulation and landing configuration from the form-finding algorithm, the initial impact of the vehicle is simulated. Because the

Venus atmosphere is very dense at the surface, it may have a significant effect on the impact scenario by adding a notable amount of drag and viscous damping to the system. Additionally, the deformation of the ground will add to the energy dissipation. However, neither factor is included due to the significant computational expense they required. Because both of these mechanisms add to the energy dissipation on impact, removing them assures that the simulation is a conservative approximation of the landing sequence. Such a simulation was used to verify that the current design was adequate for the impact conditions (i.e., the tensegrity configuration provided sufficient stiffness but was not overly constrained, no buckling of the compressive members could occur, and payload g-loading did not exceed the maximum threshold).

### **Development of a Modeling Methodology**

For the development of a modeling methodology, a sample impact scenario was devised. In this scenario a TANDEM vehicle was designed to impact the surface at 10 m/s carrying a 180 kg payload module. The vehicle used the landing configuration reported in Section 6 with a compression member length of 2 m and the shortest tension member being 67 cm. The compression members had an average diameter of 5 cm and wall thickness of 6 mm. Figures 14 shows a typical impact sequence for this model.

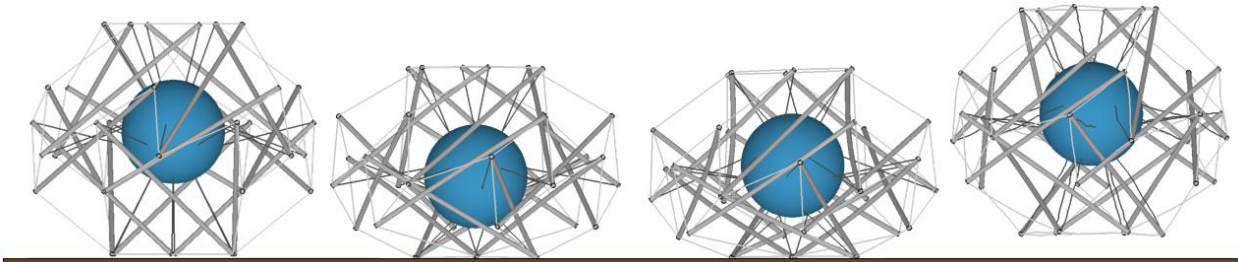


*Figure 14 Time-lapse of 0° orientation impact simulation of a 180 kg payload model at 10 m/s*

### **Modeling the Compression Members with Beam Element Formulation**

The investigations found that the introduction of a mesh refinement for the cable elements induced numerical instabilities in the models that utilized beam elements for the compression members. Thus, of the four models developed that utilized beam elements for the compression members, only two models produced results. While the beam element models required minimal computational power, neither model performed exceptionally well. Both models were able to predict similar kinematic response to the higher fidelity simulations. However, they both over-predicted the minimum clearance between the payload module and the impacting surface and over-predicted the rebounding velocity. Figure 15 shows the g-load magnitude on the payload module for the models utilizing beam elements for the compression members. The model that incorporated the rigid compression members more similarly matched the kinematic response of the higher fidelity models, but it was found that the use of rigid 1-D elements introduced a significant amount of numerical noise into the payload acceleration data. While the noise could be partially filtered out

with a low bypass filter, as seen in Fig. 15, a more preferable solution was found using shell elements to model the compressive members.

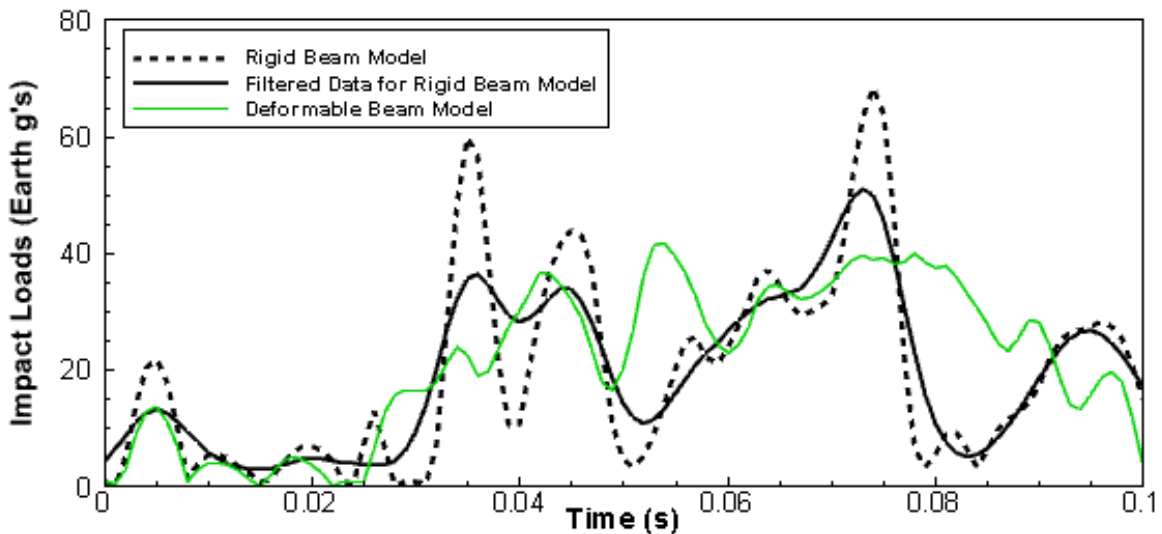


Figure 15 Magnitude of the g-load on the payload module for the models utilizing beam elements for the compression members. The Rigid Beam Model was filters at 60 Hz

#### ***Modeling the Compression Members with Shell Element Formulation***

All four of the models that utilized shell elements correlated very well with each other. All four models brought the payload to zero velocity at approximately the same time, roughly 70 ms after impact. Figure 16 shows the position of the payload module for the four models as a function of time. As expected, the minimum clearance between the payload module and impacting surface was notably smaller for the models that utilized rigid element for the compression members. This was because additional energy was dissipated through the deformation of the compression members. It can also be seen that the incorporation of the refined cable mesh resulted in only minor deviations in the kinematic response of the payload between both the rigid models and the deformable models.

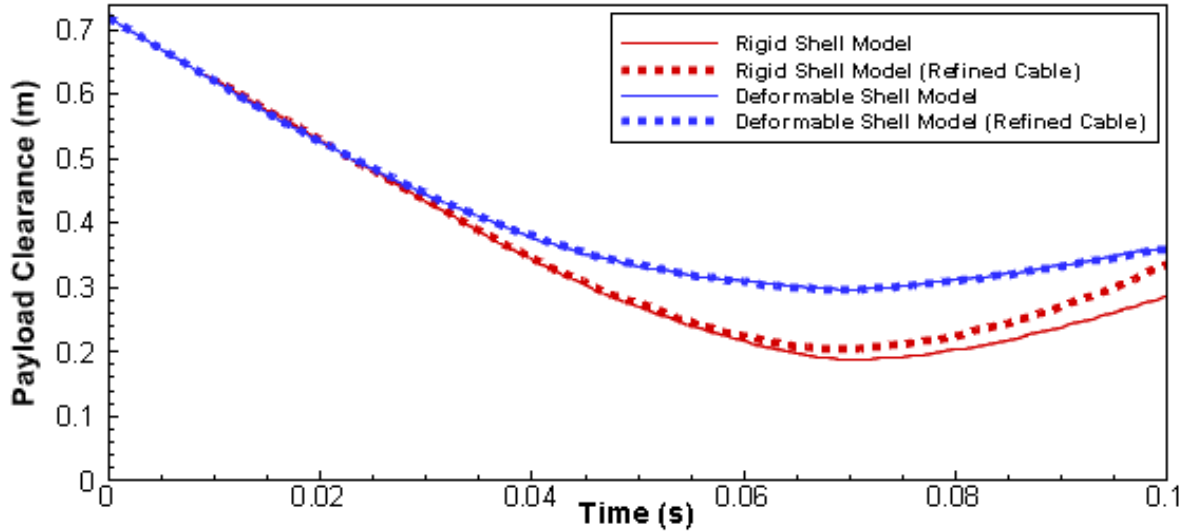


Figure 16 Comparison of the four developed impact model that utilize the shell element formulation for the modeling of the compression members

Because the system has a high number of DOFs, it can be helpful to understand the dynamic response of the vehicle on impact by considering the velocity of the payload module. For the impact models, the lateral velocity of the payload was set to 0 m/s, thus only the vertical velocity was reported. Figures 17 highlights the velocity of the payload module for the four shell element models, as well as the two beam element modules. For communication purposes, the kinematic response of the lander has been broken into three sections, as seen in Fig. 17: Initial contact from impact to 35 ms, constant deceleration starting after 35 ms, and payload rebound beginning as the payload velocity changes direction.

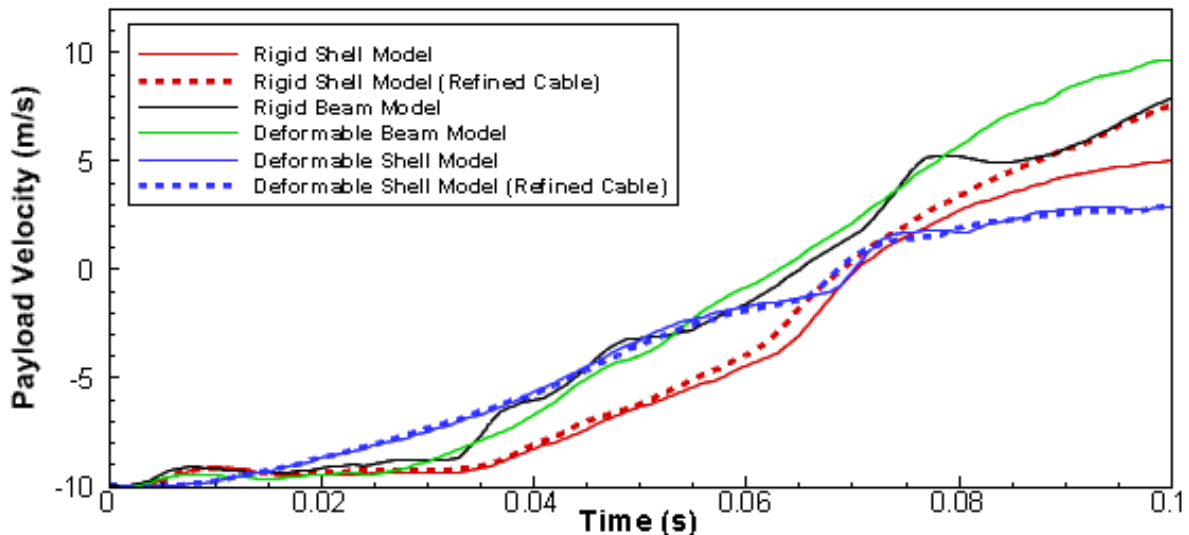


Figure 17 Comparison of all 6 impact models for the development of the analysis methodology

In the first section, initial contact, the expected response of a tensegrity lander during initial contact was captured by the two deformable shell models, which both predicted a smooth deceleration of the

## TANDEM

payload through the initial contact stage. As the vehicle contacted the impacting surface, the lower compression members began to buckle slightly. Although this minor buckling did not result in any plastic deformation, it acted as a spring, providing a near constant force on the impacting surface.

Alternatively, the beam models and both rigid shell models reported a sudden decrease in velocity and then maintained a constant velocity through that stage. This unexpected response was a result of the lower compression members recoiling after initial contact. The recoil occurred because the compression members in these models were all restricted from any non-axial deformation, thus preventing them from bending as the deformable shell elements had done. The delay in deceleration was a direct contributor to the larger stroke experienced by these models.

The next stage begins after the initial recoil of the lower members. At this point all of the models behave roughly the same, providing a relatively constant deceleration of the payload module. The constant deceleration was a result of the vehicle landing on a surface normal to its axis of rotational symmetry. Because of the configuration of the structure, the impact shockwave was evenly distributed around the structure, resulting in a near constant loading on the payload. The shockwave was able to travel through rotationally symmetric load paths from the bottom of the lander to the top with very little deconstructive interference. When the shockwave reached the top, it was reflected back down into the payload model through the upper inner cables. The reflected shockwave resulted in a sudden velocity change of the payload module, which is evident in most of the models reported in Fig. 17. The constant deceleration stage lasted different lengths of time for the individual models, but was terminated by the reflected shockwave. As the models arrested the payload, they rebounded with various velocities. The over-prediction of the rebound velocity compared to the deformable shell elements, which is the highest fidelity model, can be attributed to numerous causes, but an effect common to all of the models is that they were restricted from allowing compressive members to bend. This restriction limited the amount of kinetic energy that could be dissipated in these models, resulting in a larger rebound.

These simulations were developed to verify that a design is able to protect the payload module on impact. The clear connotation is that, for a given velocity and orientation, the tensegrity structure prevents the payload module from contacting the impact surface or any of the structure's own compression members. There is, however, an additional requirement: the tensegrity structure must protect the payload module in a manner that does not subject the payload module and its sensitive on-board equipment to excessive g-loading. One of the many benefits of TANDEM is its implementation of a low ballistic coefficient deployable heat shield, which significantly reduces the entry loads experienced by the payload module compared to traditional entries. However, the benefit of the reduced entry loads is nullified if the landing

sequence results in a significantly larger g-load. In order to develop an efficient vehicle, it must be designed such that these two primary loads are kept in a similar magnitude. Of course, there are some differences as the entry loads are endured over time and the impact loads constitute impulse loading. Thus, the impact loads can be of a slightly larger magnitude.

The velocity and position plots are useful for understanding the kinematic variance of each developed model. Understanding the differences in each scenario helps in selecting a model that efficiently balances realistic behavior and low computation expense. Figure 18 shows the acceleration magnitude of the four models that utilized shell elements to represent the structure's compression members. As seen in the velocity and position plots, Figs. 16 and 17 respectively, there is a close similarity between the refined cable models and single element cable models. Both types of models report the same trend, except that refined cable models of both reported notably lower peak loads than their single element counterpart. While the analysis may not fully reveal which of the four models best represents what would happen in a physical drop test, it indicates that the use of a single cable element to model each tension member preserves the kinematics of the payload during impact and returns a more conservative peak g-load prediction. Future work will validate this modeling methodology against a series of drop test experiments

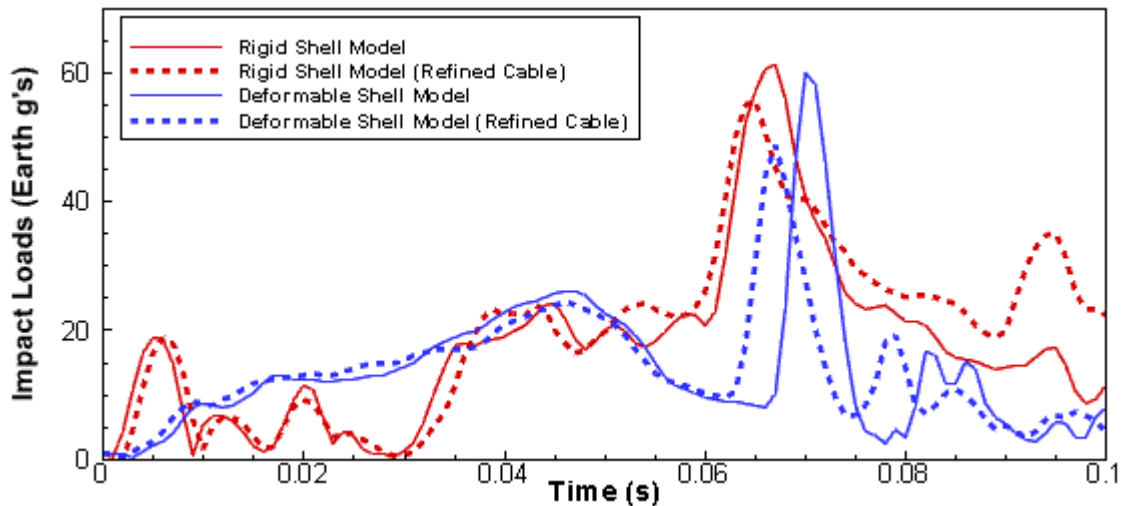


*Figure 18 Magnitude of g-load on the payload module for the models that utilize shell element formulation*

Contrasting the deformable and rigid models, a recoil on first contact is experienced in the rigid models. From Fig. 18 it is evident that in the rigid models there was not a single recoil but three distinct bounces of the lower compression members. We know from analyzing Figs. 16 and 17 that this bouncing results in a small overall clearance between the bottom of the payload and the impacting surface, but as seen in Fig. 18 it has only a minor effect on impact loads experienced by the payload. After the initial contact stage, all four models report very similar responses.

It should also be noted that if the max  $g$  experienced by the payload is the key factor, then there is very little difference between the values reported by the rigid compression member model and the one with deformable compression members. To show that this result is repeatable, the rigid and deformable single cable element models were run at three additional orientations. Figure 19 contrasts the payload accelerations of the rigid and deformable models when the models have been rotated about the  $x$ -axis  $30^\circ$ ,  $60^\circ$ , and  $90^\circ$ .

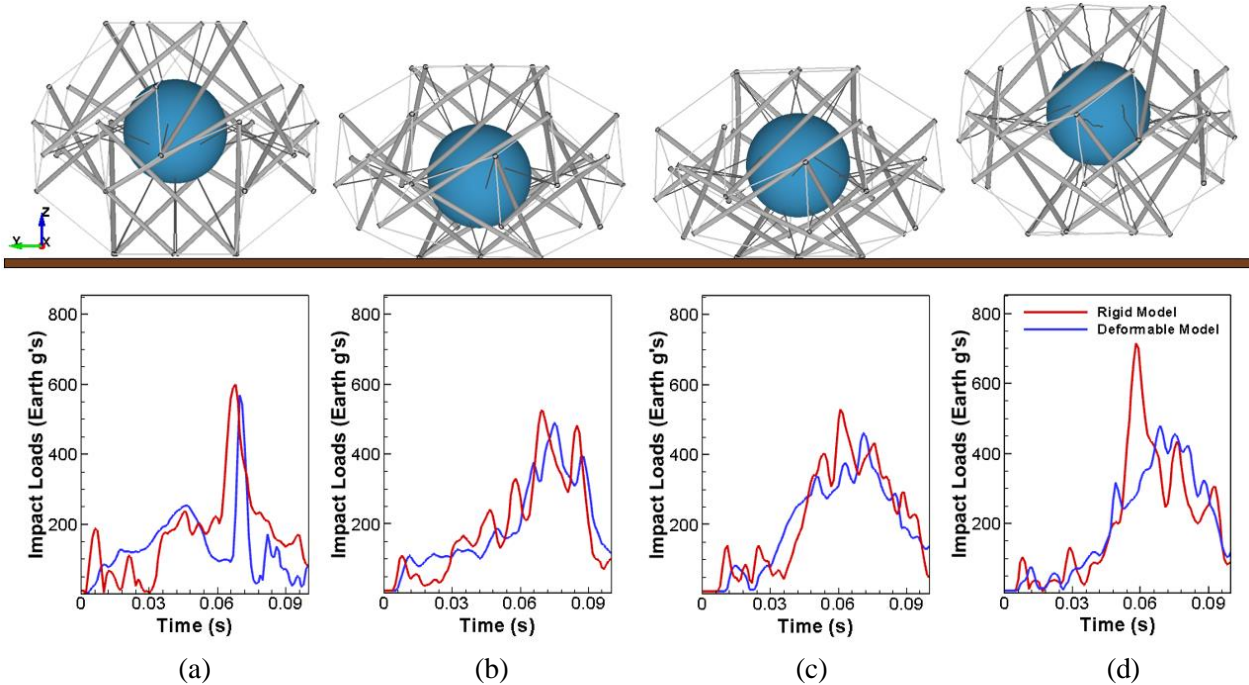


Figure 19 Parametric orientation study reveals that peak  $g$ -loading of the rigid model predicts similar result as the deformable model but at a lower computational cost

For these impact conditions, it has been shown that the peak deceleration load for the rigid and deformable models are within 12.5% of each other for three of the four orientations. This is a significant find, as the deformable model takes approximately 4 times the computational power as the rigid model. Thus, for most simulations, the lower computational expense model can be used. There are exceptions where the rigid model does not match well with the deformable model, as seen in Fig. 19 (d). The difference in peak load is a result of the payload module contacting a compression member in the rigid model but not in the deformable model. As shown in Fig. 16, the rigid model over predicts the maximum displacement of the payload module. Additionally, in the deformable model when the compression members bend, they tend to bend away from the payload module. In light of this, the rigid model is a conservative model for impact analysis, provided the compression members are well-designed. Thus, if the rigid body simulation predicts the payload module contacts one or more of the compression members or the impacting surface, a deformable model should be run to confirm that conclusion. In many cases, when the rigid body model predicts a contact, the deformable body shows a large clearance as seen in Fig. 20.

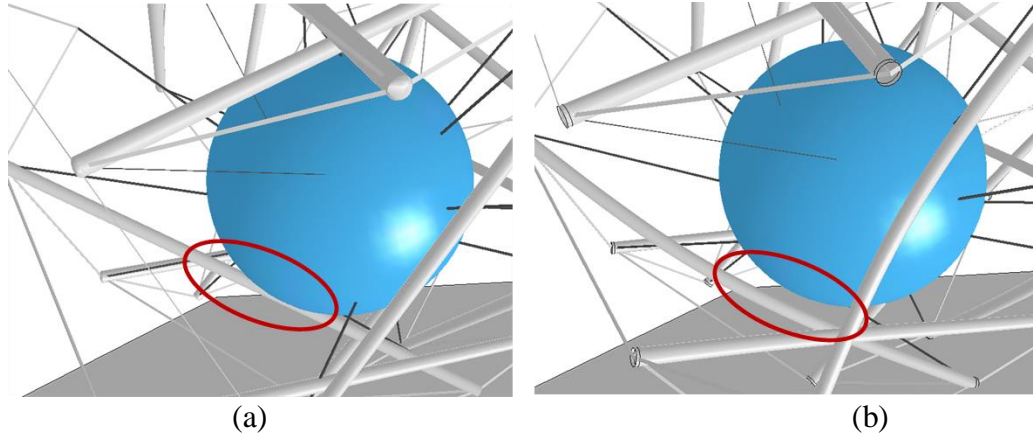


Figure 20 Comparison of rigid (a) and deformable (b) compression members models shows that the rigid model predicts false collisions

From this analysis of various modeling methodologies, it was found that the use of beam elements to represent the compression members of a tensegrity lander, in the method described, is not feasible. The beam elements resulted in inaccurate kinematics and excessive numerical noise in acceleration data. An alternative method of using beam elements, proposed by Rimoli<sup>48</sup>, may yield more favorable results, but this methodology was not attempted in this study.

### Parametric Impact Study

Using the developed modeling methodology, a series of landers were developed to find any trends that may exist. Two 1 m diameter payload modules were used, one weighing 180 kg in total and the other weighing 260 kg. Various efficient, but not optimized, lander designs were developed based on three different impact velocities: 10, 20 and 30 m/s. Table 6 reports the dimension and masses of each vehicle designed.

Table 6 Parametric TANDEM Designs Based on Payload Mass and Impact Velocity

	180 kg Payload Module			260 kg Payload Module		
	10 m/s	20 m/s	30 m/s	10 m/s	20 m/s	30 m/s
Rod Length (m)	2.0	2.5	3.0	2.0	2.8	3.0
Rod Mean Diameter (cm)	5.0	7.8	11.5	5.0	8.5	11.5
Rod Wall Thickness (cm)	0.6	0.6	0.6	0.6	0.6	0.6
Rod Mass (kg)	11.0	186.0	33.6	11.1	22.8	33.6
Total Vehicle Mass (kg)	338.3	531.0	696.7	463.0	672.0	889.4
Mass w/o Payload (kg)	158.3	351.0	516.7	203.0	412.0	629.4
Maximum G-load on Payload	59.9	96.9	224.4	35.3	87.0	192.9

The total lander masses from Table 6 were plotted and fitted to a trend line, as shown in Fig. 21. As can be seen, there appears to be a linear relationship between impact velocity and total mass of the

vehicle for a given payload module mass. This is complementary to the finding reported by Agogino et al. in their NIAC report that the mass of a tensegrity structure grows linearly with compression member length, unlike airbags which grow with the square of the radius<sup>49</sup>. This statement was made in the context of small, low mass tensegrity structures impacting at a single velocity. The work presented in this study shows how the design will scale as the impact velocity increases. Furthermore, as the tensegrity vehicle increases in size, the compression members are more susceptible to buckling, due to a longer rod length. Thus, as a tensegrity structure is scaled up, the radius of the compression members must be increased, as well as its length. Our analysis takes all of this into account and still shows that the linear scaling relationship appears to hold up.

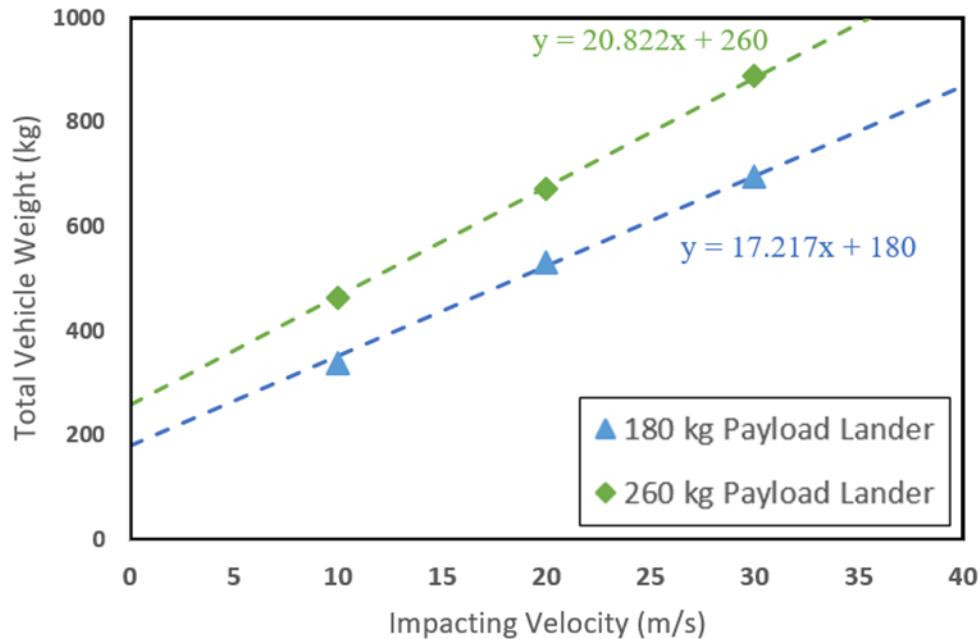


Figure 21 Scalability of TANDEM vehicle mass has a linear relationship with impact velocity

### Impact Globe

In order to demonstrate omnidirectional protection provided by TANDEM, a large parametric study was performed to impact the TANDEM model at various orientations. Each orientation was systematically selected to ensure an even sampling distribution across all possible orientations. Two models were selected for this analysis: the 180 kg payload model impacting at 10 m/s and the 260 kg payload module impacting at 20 m/s.

This parametric impact study resulted in a “globe” broken up into the latitudes and longitudes correlating to each impact simulation. Each point on this map represents the peak g-load experience by the payload for a given orientation. The south and north polar regions, in Fig. 22, correlate to the bottom and top face of the TANDEM vehicle, respectively.

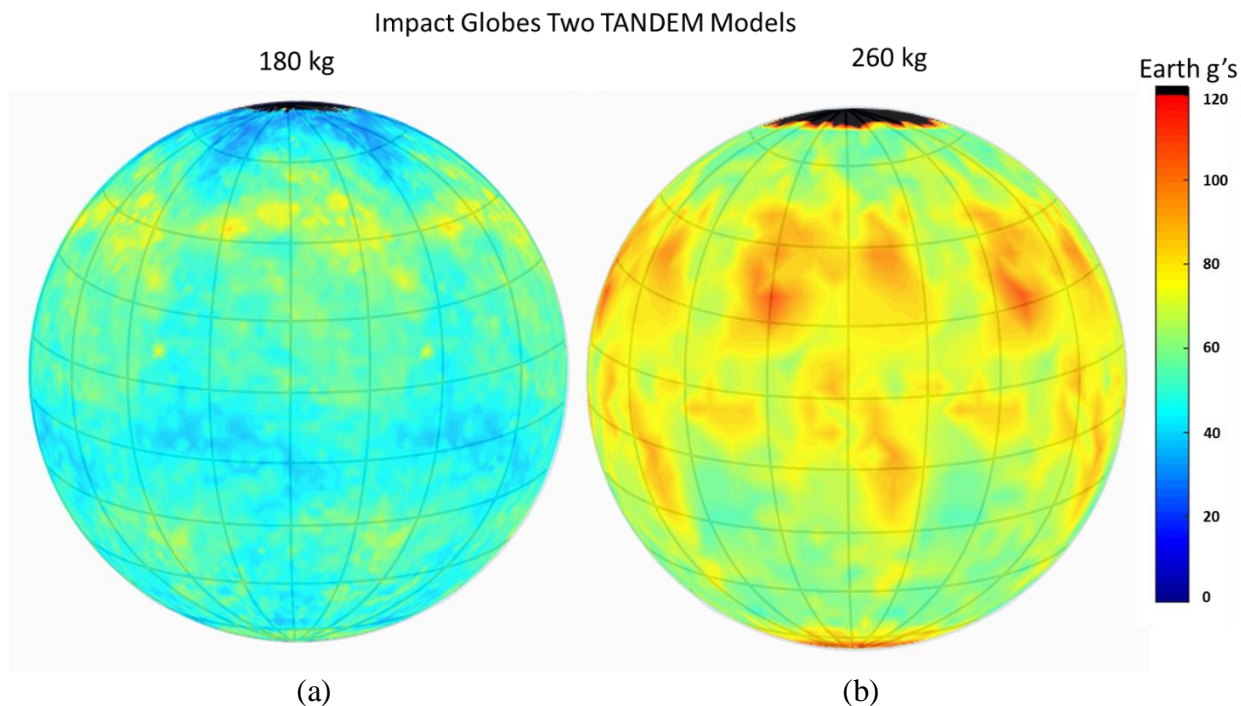


Figure 22 Impact globes of two TANDEM models, (a) the 180 kg payload impacting at 10 m/s (b) 260 kg payload impacting at 20 m/s

The biggest takeaway from Fig. 22 is that an impact simulation has been run and analyzed for nearly every possible impact orientation. Furthermore, nearly all of the tested impact cases report a peak load on the payload module less than 120 g's. When the vehicle was completely inverted, however, this analysis predicted that the payload module would come into contact with the surface, shown in black on the northern poles of Fig. 22. While the impact occurred at a low velocity (approximately 2 m/s), it revealed a potential gap in the omnidirectional protection provided by TANDEM

Investigations of this weak point in the otherwise fully protective outer tension network revealed that the cause of the weakness was in the selection of the impact configuration and not a problem inherent to the concept itself. Further investigations will provide a new landing configuration that does not present the same weakness as the current configuration.

## Obstacle

As a primary goal of this investigation was to explore the feasibility of performing landed science in the Tessera regions of Venus, it is important to explore very unfavorable landing conditions. Thus a boulder impact investigation was performed for two of the developed vehicle models: the 180 kg payload model impacting at 10 m/s and the 260 kg payload module impacting at 20 m/s. An investigation of radar reflectivity from Magellan and the Arecibo observatory suggest that Tessera regions can have surface

roughness on the order of 10 to 50  $cm^{50}$  while the VITaL mission concept was designed to land on a boulder as large as 1.3  $m$  tall<sup>25</sup>. So for this investigation, the two TANDEM vehicles were impacted on a 1  $m$  tall rigid obstacle.

For the smaller vehicle an example impact was simulated where 3 of the 6 lower compression members were above the obstacle. Because the vehicle is held in a constant state of tension, even though only half of the lower compression members made contact with the impacting surface, the shape of the vehicle at its maximum stroke was nearly the same as its shape when it impacted a flat surface. However, because the landing was not over a flat surface, the minimum clearance between the payload model and the impacting surface was reduced from 30  $cm$  in the level impact case to 12  $cm$  when landing on an obstacle, as shown on Fig. 23.

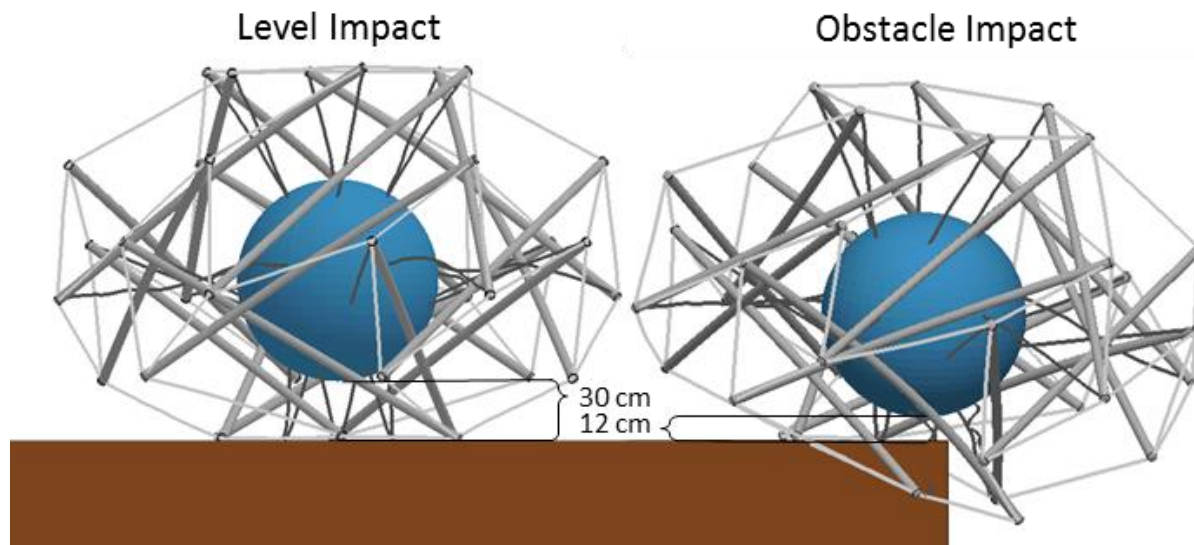


*Figure 23 Comparison between the minimum payload clearance when impacting on a flat surface versus impacting on an obstacle*

Since the payload clearance was reduced, the impact load on the payload module were also reduced significantly as a result of impact on a non-level surface. As discussed above, in the level impact case, the shockwave is reflected from the top of the vehicle down into the payload module through the upper inner cables. However, because the landing surface in this case was non-level, the shockwave was not transmitted through axisymmetric load paths. Thus, when the shockwave reached the top face it had largely dissipated. As a result, the peak  $g$ -loading on the payload module was reduced by over 15  $g$ 's. Figure 24 shows a comparison of the impact loads for the level impact case and the boulder impact case. Note that the results in Fig. 24 were obtained using the vehicle model which incorporates deformable compression members and a cable element refinement.

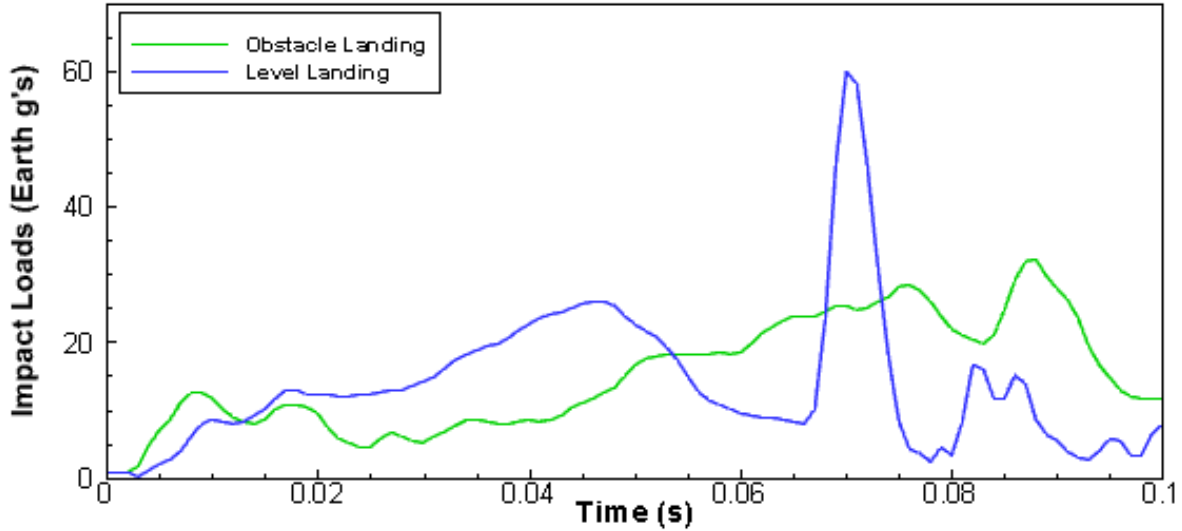


Figure 24 Comparison of the deceleration load related to impacting on a flat surface and a non-level surface given a 180 kg

For the case where the larger lander impacted the surface, a scenario was selected where only two of the lower six compression rods contacted the impacting surface. As in the previous example, the uneven impact surface resulted in a significant reduction of impact loads. The payload module in this analysis saw a decrease of nearly 16 g's compared to the level impact case. However, in this case, when the vehicle impacted the surface, one of the lower compression members struck the edge of the boulder. With the end points of the compression member constrained by the tension network, this non-axial load created a large bending load on the member, resulting the permanent deformation and local buckling of the beam. Figure 25 (a) shows the Von Mises stress on the vehicle as it impacts the boulder and Fig. 25 (b) shows the post impact deformation of the buckled compression member.

## TANDEM

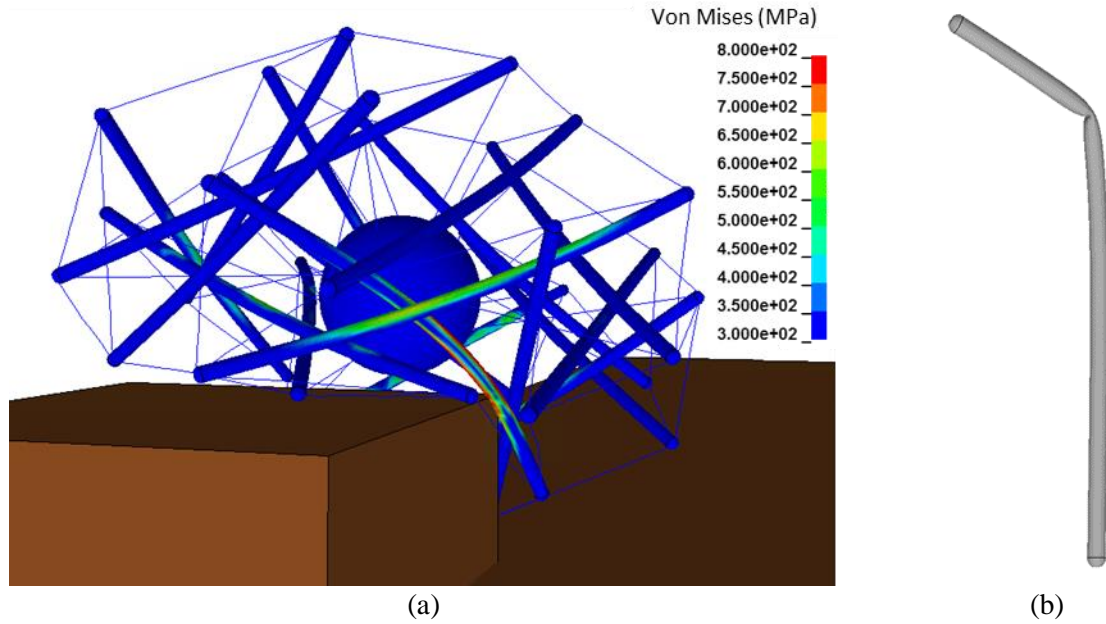


Figure 25 Buckling of one compression member as a result of landing on an obstacle (a) von Mises stress just before rod buckling occurred (b) post buckling shape of compression member

It is important to notice that even with the failure of a compression member, the stability of the tensegrity structure remained largely unaffected, and the payload module remained isolated and protected. As shown in Fig. 26, after the bounce, when the vehicle impacted the surface again, no negative impact characteristics were noticed due to the buckled compression member. This is due to the redundancy inherent in the tension network. Even when one component is damaged or removed, the loads are redistributed through the tension network so that the payload is protected.

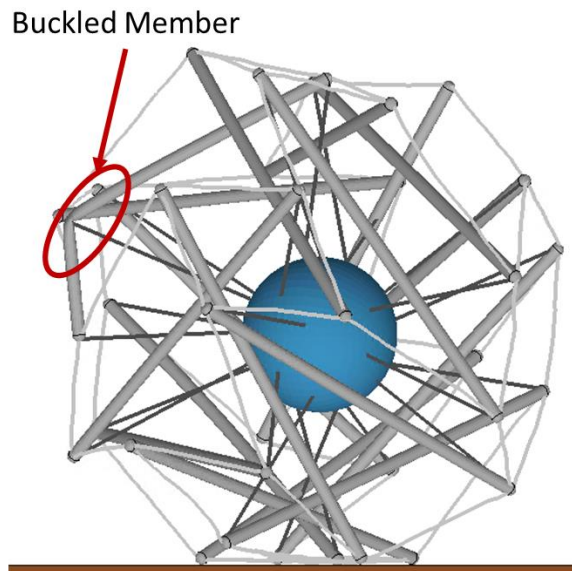
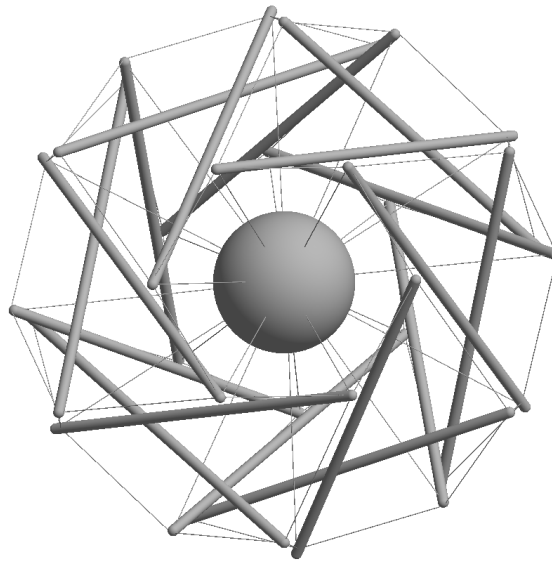


Figure 26 TANDEM still protects the payload module even with the failure of a compression member

## **9. Control and Locomotion Investigation**

Because TANDEM is designed around a tension network, control is a nonlinear problem. The length of each tension member in TANDEM is controlled by a stepper motor, but the position and orientation of the cable is dependent on the position and orientation of the tension and compression members connected to it. As can be seen in Fig. 27, the structure is rotationally symmetric about its vertical-axis. In this study it was decided that the baseline model of TANDEM would be comprised of six sections. However, alternate versions of TANDEM can be developed by increasing or decreasing the number of rotational sections based on the mission requirements.



*Figure 27 Top view of TANDEM vehicle reveals that it is rotationally symmetric*

Three types of control strategies were developed in this work in order to change the configuration of the vehicle throughout a given mission. Each of these strategies is used for different maneuvers throughout the EDLL sequence. The control strategies were classified into categories based on the type of configuration changes desired. These classifications were titled: CG offset, symmetric, and non-symmetric. The CG offset maneuver can be used on entry to create a non-zero lift to drag ratio. Additionally, it can be used on descent to steer the vehicle in various directions. Symmetric configurations are used in transitional stages of the EDLL sequence, e.g. the deployment of the heat shield or the transition from the deployed configuration to the descent configuration. Lastly, non-symmetric configuration changes are predominantly used in on-the-ground locomotion.

The CG offset maneuver is the simplest of the available control strategies, because it does not require reconfiguration of the outer tensegrity structure. Because the outer structure is already a stable tensegrity structure in itself, the inner cables can be adjusted independently of the outer cables. This enables

direct control of the position of the payload module, and thus the CG of the entire system, by controlling only the inner cables.

Symmetric control strategies are slightly more difficult. In these transitions, each rotational section of the structure must go through the same configuration change. This significantly reduces the number of degrees of freedom available in the system. There are 3 rods, 9 outer cables, and 4 inner cables in each periodic section. Figure 28 shows a single section of the tensegrity structure. For simplicity of the diagram, the cables connecting the payload module to the outer tensegrity structure (i.e. the inner cables) were omitted.

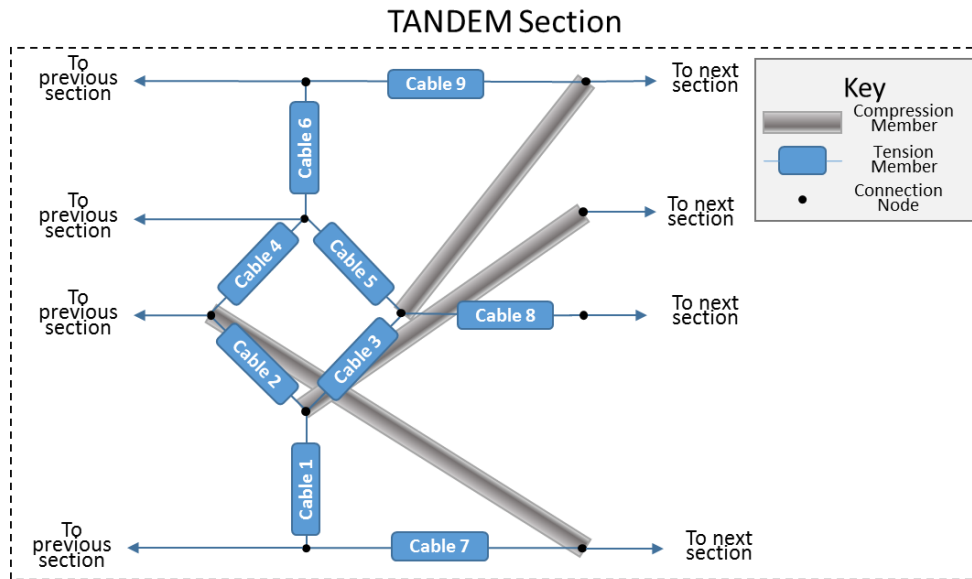


Figure 28 Schematic view of a single rotational section of TANDEM's tension network

For symmetric configuration changes, the primary goal is to transition the vehicle's shape to prepare for the next stage of the EDLL sequence. Assuming that the vehicle's current configuration and its desired configuration are known, the input required of each stepper motor can be calculated using the form-finding algorithm, discussed in Section 6. The form-finding algorithm uses the length ratio of each tension member in a rotational section as input and delivers the tension member's position, orientation, and actual length. By linearly varying the input parameters from the initial configuration to the final configuration, the form-finding algorithm provides nonlinear changes in tension member lengths. This provides the input parameters required for each actuator in order to control the shape of the structure from one stable configuration to another. Figure 29 shows the change in length of each tension member for the symmetric transition from the stowed configuration to the deployed configuration. Each bar in Fig. 29 shows the transition of an individual tension member from the initial configuration to the final configuration. As can be seen in Fig. 29, the length of each cable varies nonlinearly as the configuration of the vehicle changes.

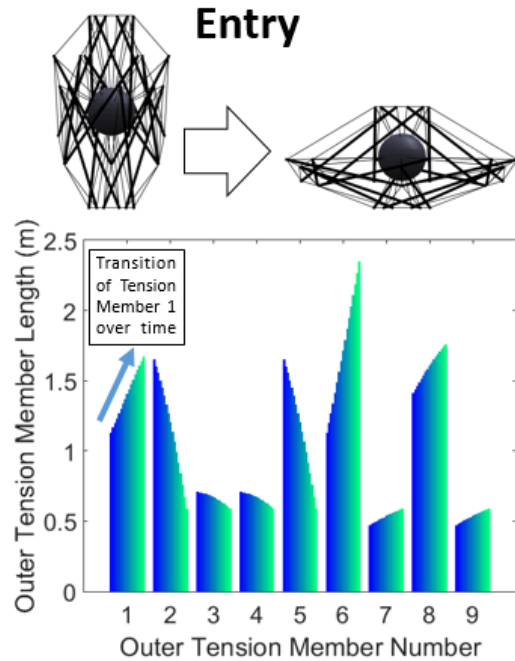


Figure 29 Nonlinear transition of cable length from the stowed configuration to the deployed configuration

Figure 30 shows the change in tension member length for two other symmetric configuration changes. The configuration change of TANDEM before entry, descent, and landing make up the three primary uses of the symmetric control strategy.

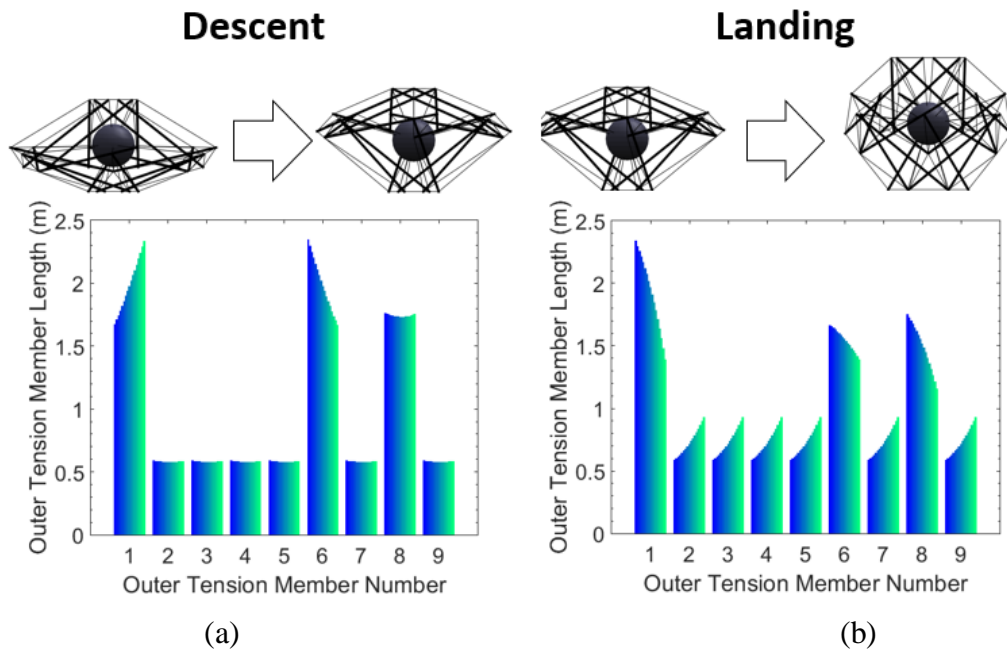


Figure 30 Variation of cable lengths used in the symmetric configuration change before (a) descent and (b) landing

## TANDEM

Non-symmetric control is the most challenging. Unlike symmetric configuration changes, non-symmetric control strategies must account for the dynamics of the configuration change. The typical goal of non-symmetric configuration changes is for the implementation of surface locomotion through a variety of gaits. For gait development and simulation, NTRT simulator was used. NTRT was developed largely by the Dynamic Tensegrity Robotics Lab at NASA Ames for research on the design and control of tensegrity robots. NTRT is a tensegrity simulator built to run in the Bullet Physics Engine, version 2.82. While fully developed control system and advanced gait study are outside of the scope of this preliminary study, a gait development methodology was selected and discussed below. Additionally, a demonstration of a simple rolling gait is presented as proof of concept for surface locomotion.

In NTRT, the length of each cable can be actively controlled. However, because the structure's shape is held by a tension network, changing a single tension member may propagate through the structure, causing additional deformation and nonlinear force propagations. Due to its complexity, controlling tensegrity robots typically require advanced control systems. Ongoing work focuses on utilizing NTRT's controller libraries to implement Central Pattern Generators (CPGs) and machine learning frameworks to develop advanced locomotion gaits.

CPGs, are neurons involved in motor control, which are used to create a rhythmic pattern. These patterns express some of the ways that a basic process can be repeated over time. Examples of these rhythmic patterns are seen in Nature for various types of locomotion include walking, swimming, or flapping flight. In most living organisms, neurons in the central nervous system act as a CPG to engage in these movements<sup>51</sup>. These same rhythmic patterns are of great interest as a method to control autonomous vehicles, such as our TANDEM tensegrity structure.

For the TANDEM application model, a central circuit generates the rhythmic patterns for each motor neurons to excite the muscles (or actuate the tension members) and produce movement. Each CPG node corresponds to each actuator within the structure. In this configuration, the CPG generates gaits based on the connectivity of each node and the differences in phase between the compression members and the supporting tension members. The governing equations for each CPG node,  $i$ , in this system are listed below as a function of its relationship to each of its neighboring nodes,  $j$ .

$$\dot{\theta}_i = 2\pi v_i + \sum_j r_j w_{ij} \sin(\theta_j - \theta_i - \varphi_{ij}) \quad (20)$$

$$\ddot{r}_i = a_i \left[ \frac{a_i}{4} (R_i - r_i) - \dot{r}_i \right] \quad (21)$$

$$v_i = r_i (\cos(\theta_i)) \quad (22)$$

Equation 20 is used to determine the phase of the CPG and Eq. 21 determines the amplitude. The overall velocity of the impedance controller is determined by Eq. 23. In these equations  $v_i$  is a frequency term,  $r_j$  represents the amplitude of the coupled node,  $w_{ij}$  is the coupling weight and  $\varphi_{ij}$  is the phase offset. Furthermore,  $R_i$  is a set point for amplitude,  $a_i$  is a positive constant,  $R_i$  and  $v_i$  are each one parameter, or represent the combination of an offset, a gain, and the command itself<sup>52</sup>.

In order to select these CPG constants, a Monte Carlo simulation will be used to vary the CPG constants over a predefined range. The effectiveness of each set of constants will be measured by the overall displacement of the center of mass of the structure over a finite length of time. The energy imparted to the system may also be considered in the selection of the most effective gait developed by the Monte Carlo run. After the design space is explored by the Monte Carlo simulation, a genetic algorithm will be used to iterate over the best result from the Monte Carlo, to see if a better set of constants can be found.

A basic locomotion kinematics are shown in Fig. 31. The rolling gait demonstrates simple locomotion for traversing flat surfaces. There are three steps in the rolling gait. The first step is to raise the CG of the vehicle by reeling in the upper inner cable and unspooling the lower inner cables (frame 1). Next, the inner lateral cables are used to shift the payload module a small amount in the desired direction of the locomotion. The shift in the vehicle's CG causes the rover to begin to fall over (frame 2). After the vehicle had rolled onto its side, the bottom circumferential cables were extended, allowing the vehicle to roll further (frame 3). As a result of this maneuver, the vehicle rolls 180° such that it rests on its top face (frame 4). The procedure can then be repeated by reversing the roles of the upper and lower cables.

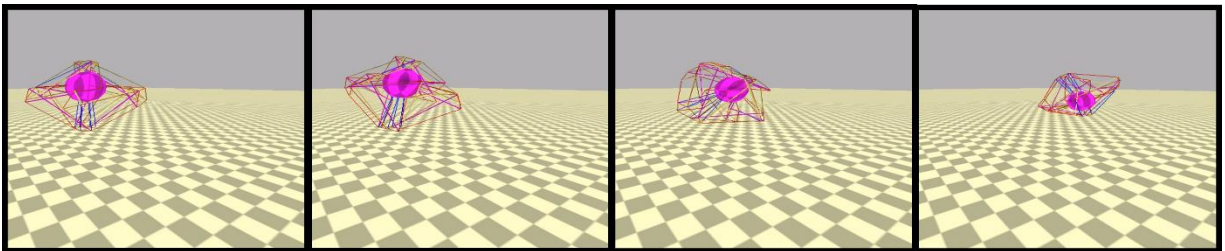


*Figure 31 Time-lapse of preliminary locomotion study*

## **10. Conceptual Mission to Venus**

The most recent Decadal Survey has listed a Venus In-Situ Explorer (VISE) type mission as a candidate for a New Frontiers mission<sup>2</sup>. Venus presents a great exploration opportunity, as it is our closest planetary neighbor. Venus is similar to Earth in both size and location in the solar system, yet it is profoundly different in many other aspects regarding habitability. There is a significant scientific interest in exploring the mysteries of the greenhouse gases and runaway climate change present in the Venusian atmosphere. Understanding Venus' atmosphere will help increase the knowledge of Earth's atmosphere.

## TANDEM

Exploring the difference in these two planets will greatly further our intuition of other planetary systems and will aid in our search for life in the universe. Yet, exploring Venus presents a number of severe engineering challenges including the extreme temperature and pressure at the planet's surface, the highly corrosive atmosphere, and lack of terrain resolution caused by dense permanent cloud layers.

The Decadal Survey has stated, “There is a critical future role for additional VISE-like missions to a variety of important sites, such as Tessera terrain.”<sup>2</sup> The concept mission developed for the Decadal Survey to explore this region was the VITaL mission<sup>25</sup>. However, their study showed that the entry loads were too high for the Raman/LIBS spectrometer and that the terrain of the Tessera region can be “viewed as largely inaccessible for landed science due to its known roughness.”

TANDEM provides the same scientific experimentation capabilities that were proposed for the VITaL mission, with estimated reduced mass, while eliminating the identified risks associated with entry loads and very rough terrain. Surface locomotion is the additional primary benefit that TANDEM provides over other concepts. Thus, TANDEM’s unique multifunctional infrastructure presents a robust system to address some of the Decadal Surveys most pressing questions. The EDLL sequence for this mission is summarized in Fig. 32.

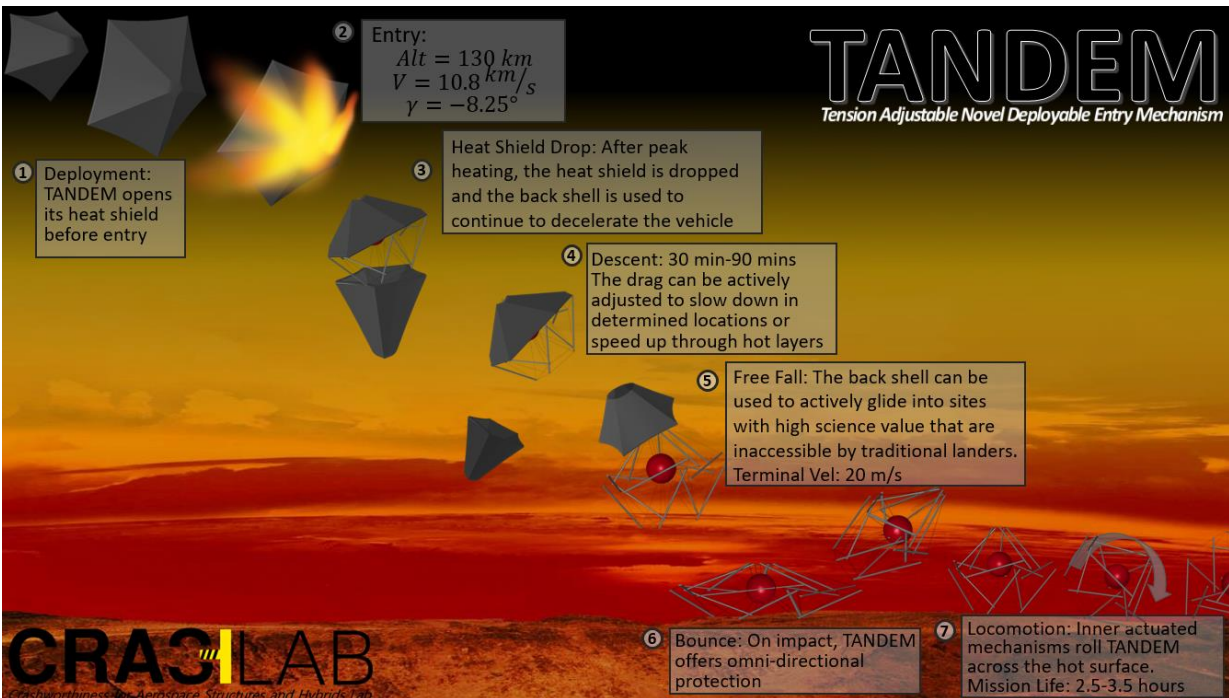


Figure 32 EDLL sequence for TANDEM mission to Venus

The design of a TANDEM vehicle, like many EDL concepts, is an iterative process. There are two sections in the EDL sequence where the vehicle is exposed to a high g-loading: during entry and on landing. In order to achieve an efficient design, it is important that neither the entry vehicle nor the lander/rover be

over-designed. Thus, the vehicle should be designed such that both of these g-loadings be approximately equal to each other.

For a ballistic entry, it is important to notice that the flight mechanics code (i.e., Eq. 1) is a function of the ballistic coefficient ( $\beta_{entry}$ ) and not a detailed design of the vehicle. Thus, a preliminary flight mechanics analysis is performed with  $\beta_{entry}=47 \text{ kg/m}^2$ . Given an entry velocity of  $10.5 \text{ km/s}$  and an entry flight path angle (EFPA) of  $8.5^\circ$ , the FMC predicted a trajectory with an entry g-loading of 65 Earth-g's. Approximate ballistic coefficients of  $\beta_{descent}=45 \text{ kg/m}^2$  and  $\beta_{lander}=1900 \text{ kg/m}^2$  are assumed to calculate the terminal velocity of the vehicle at various stages. The descent stage could reach terminal velocity as low as  $3.5 \text{ m/s}$ , but when the backshell is released the lander will accelerate to a velocity of  $23 \text{ m/s}$ . Figure 33 shows the details of vehicle trajectory.

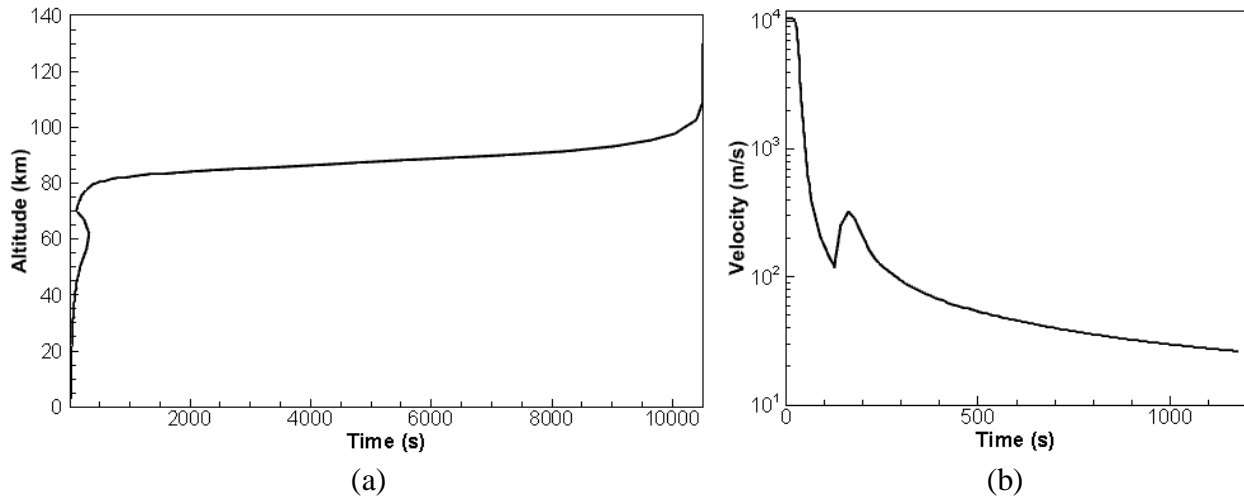


Figure 33 The descent history of the detailed vehicle concept (a) altitude versus time (b) log of velocity versus time

### Scientific Instruments and Payload Module

The payload module selected for this mission was the same design as used for the VITaL mission concept<sup>25</sup>. This payload module was selected for a number of reasons. The included instrument suite was carefully selected to answer as many Decadal Survey question as possible. Furthermore, the use of the same payload module enables a direct comparison to be made between the VITaL concept and TANDEM. Appendix B shows details on the comparison between TANDEM and other Venera-class landers such as VITaL.

The scientific instruments include, three cameras, a Raman/ LIBS (Laser Induced Breakdown Spectrometer), Neutral Mass Spectrometer, Tunable Laser Spectrometer, magnetometer, and an atmospheric analyzer (consisting of a temperature sensor, a pressure transducer, anemometer, and an

## TANDEM

accelerometer). All of the instruments, except Raman/LIBS, currently exist at a high TRL and can be designed to survive an extended exposure to 200 g's, the load expected during entry in the VITaL mission.

Part of the reason that the Raman/LIBS is at a lower TRL than the other instruments is because it was expected to measure surface composition from 2.5 m away. This distance combined with the high entry loads of the VITaL entry, create a substantial design problem. The VITaL cost estimate sets \$20M for technology development, with most of this cost being attributed to the development of the Raman/LIBS<sup>25</sup>. The use of TANDEM can substantially simplify the design requirement surrounding the Raman/LIBS. Firstly, the entry loads with TANDEM are 135 g's less than that of VITaL. Furthermore, because TANDEM can locomote, the Raman/LIBS will not need to make measurement from 2.5 m in order to get a wide sampling distribution. These two aspects of TANDEM greatly reduce the sensitivity required for that instrument's operation and will thus accelerate the elevation of its TRL. Figure 34 shows an example



Figure 34 Section cut of the Payload Module

### Vehicle Design

As the terminal velocity and payload module for this first iteration was similar to that of model developed for the 20 m/s impact with a 260 kg in Section 8, the same lander design was used. With the design of the lander fully defined, the entry vehicle was developed. Many of the values used to define the TANDEM aeroshell were based on the similarly designed heatshield from the ADEPT-Vital mission<sup>3</sup>. A comparison between the ADEPT and TANDEM concepts was provide in Appendix A. The length of the heatshield struts and the diameter of the entry vehicle were scaled in order to match the ballistic coefficient of the preliminary run. The final diameter of the deployed heatshield was 4.5 m with a cone angle of 70° and strut lengths of 2 m. Table 7 contains a mass breakdown of the whole TANDEM vehicle. The “Overall Deployment System” is an additional motor-driven cable system for the pretensioning of the heat shield. This deployment should be entirely covered by the locomotion system. However, the system was included in the design of TANDEM as an additional margin if the locomotion motors do not produce sufficient torque to fully pretension the heat shield to the required tension.

Table 7 TANDEM's Master Equipment List. Many values relating to the Aeroshell were based on values from the ADEPT-VITaL Concept<sup>3</sup>

Mass List	TANDEM		
	CBE	Growth	Predicted Mass
	1007 kg		1300 kg
<b>Aeroshell</b>	<b>338</b>		<b>432</b>
Heat Shield	134		174
Nose Cap & Lock Ring	61	0.3	79
Ribs & Bearings	23	0.3	30
Joint Hardware	10	0.3	13
Carbon Cloth	40	0.3	52
Rigid Nose TPS	71		85
Nose TPS	50	0.2	60
Ribs TPS	12	0.2	14
Aft Cover TPS	9	0.2	11
Backshell	30	0.3	39
Mechanisms & Separation	86		112
Overall Deployment System	60	0.3	78
Stowed/Deployed Latched	19	0.3	25
Avionics & Power	17		22
Avionic Unit	4	0.3	5
Harness	5	0.3	7
Power Unit	8	0.3	10
<b>Lander</b>	<b>669</b>		<b>868</b>
Scientific Payload	37	0.3	48
Thermal	66	0.3	85
Power	12	0.3	16
Comm, Avionics & Electronics	24	0.3	32
Structure	120	0.3	154
Landing System	410	0.3	533

A common practice in concept design work is to add a 30% growth margin to the original design as seen done in Table 7. This added margin will affect the ballistic coefficients of the vehicle. To insure that the aerothermodynamic fluxes and loads are not excessively increased the radius of the deployed heat shield was increased by 10 cm to return the entry vehicle back to a ballistic coefficient  $47 \text{ kg/m}^2$ . With the TANDEM vehicle fully developed, the flight mechanics code was run using the predicted masses from Table 7. During entry, the modified Newtonian method was used to calculate the aerodynamic loads on the

heat shield. Figure 35 (a) shows that the heatshield needs to be able to withstand no more than 58.25 kPa on entry. While Fig. 35 (b) shows a peak heat flux of 333 W/cm<sup>2</sup> and a total heat load of 4634 J/cm<sup>2</sup>.

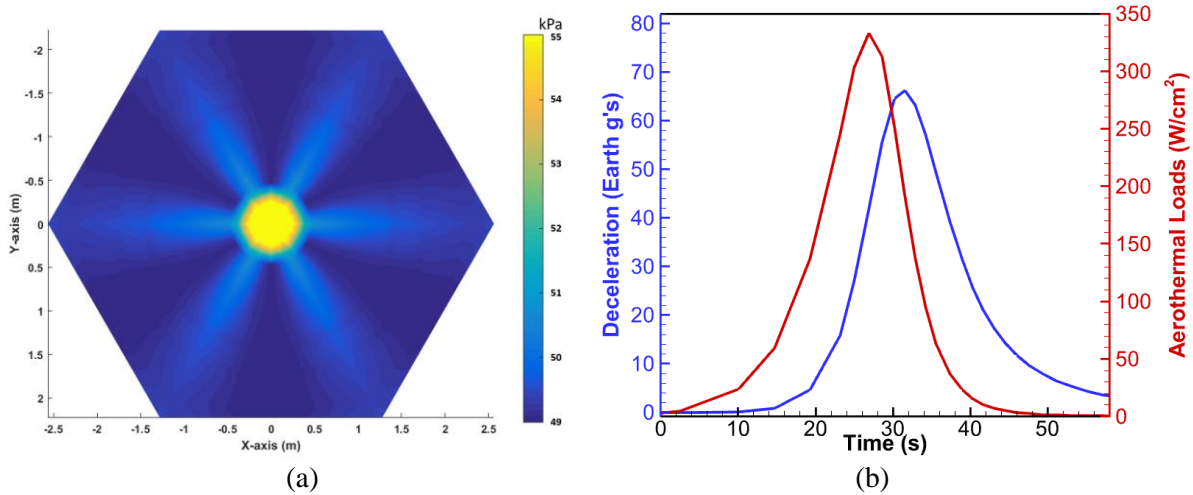


Figure 35 Results from the flight mechanics code (a) maximum aeroloads at peak deceleration. (b) g-loading and aerothermal loads

The 30% mass margin did increase the terminal velocity of the vehicle to 25 m/s as predicted in Section 7. With the added mass margin and the new terminal velocity, a new impact analysis was performed. Figure 36 show the von Mises stress plot of the compression members at the time of max stress. The maximum stress in the compression members was 800 MPa.

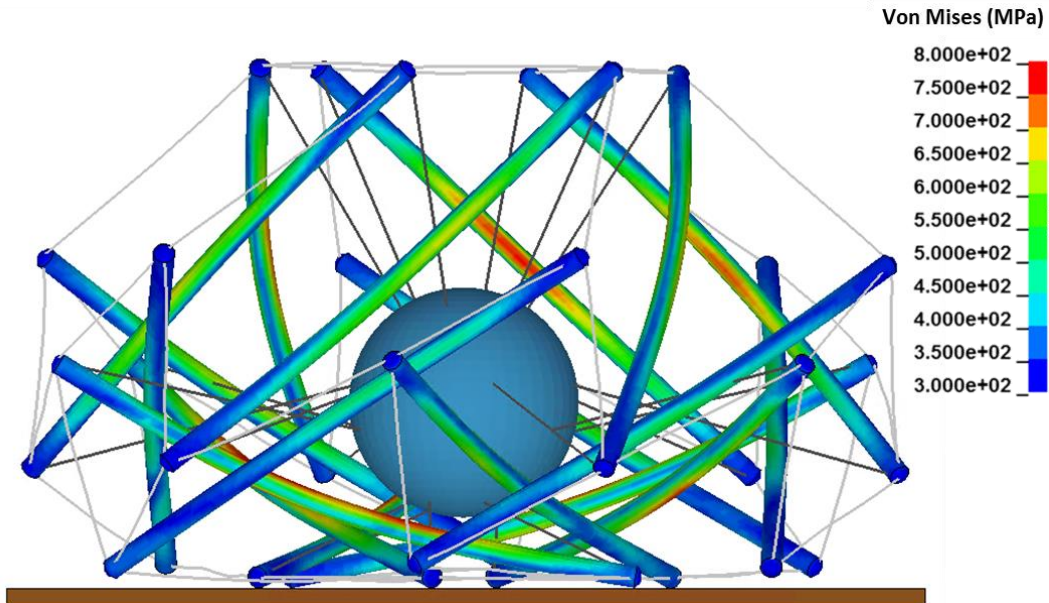
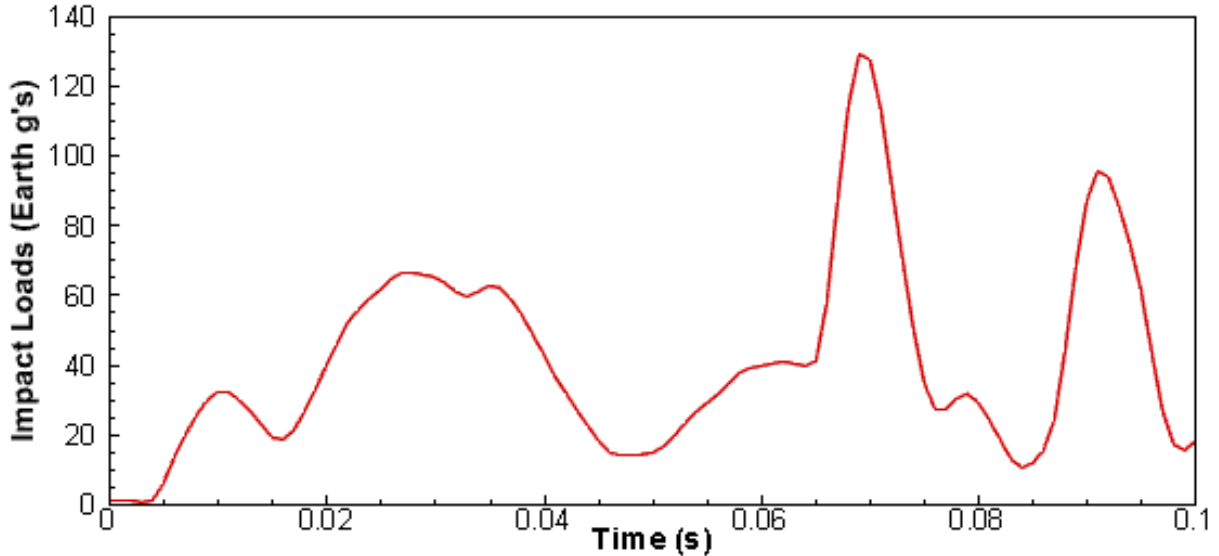


Figure 36 von Mises stress on compression members for the impact of predicted mass model

Figure 37 show the magnitude of the impact loads experienced by the payload module. The max g-load on the payload was 129 g's. While this is nearly double the max deceleration experienced on entry, its duration should be abrupt enough that no damage is done to the scientific payload.



*Figure 37 Deceleration of the payload module of the predicted mass vehicle at 25 m/s*

## **11. Conclusion and Continuing Work**

The TANDEM concept provides a high level of adaptability and controllability, which can be utilized throughout the EDLL sequence. This opens all new avenues in maneuvering options during EDLL, including lifting/guided entry, guided descent, and hazard avoidance. Beyond the controllability and maneuverability that TANDEM displays on entry and descent, TANDEM is designed to land at any orientation and can traverse significantly rougher terrain than previous rovers. This means new landing sites can be reached. Instead of landing in low risk areas then traveling to the closest area of scientific interest, missions using TANDEM can land directly in the region of interest. Thorough impact analyses have shown promising results that indicate that TANDEM can safely enable landed science in the Tessera regions.

The unique multifunctional infrastructure is a critical feature that sets TANDEM apart from the current state of the art. Further, in addition to the myriad of functionalities it offers, TANDEM has displayed a significant mass saving compared to other contemporary concepts. As discussed in Appendices B and A respectively, the predicted mass of the detailed TANDEM lander design is 190 kg less than the predicted mass of the ADEPT-VITaL lander, with an 800 kg overall mass reduction for the whole entry vehicle.

Research and development on the TANDEM concept continues. A number of ongoing research were mentioned earlier in this report. Advanced locomotion studies, utilizing CPGs and the machine learning methods, as described in Section 9, are priority areas of focus. Additionally, an investigation into the development of high temperature radio transmitters and receivers is underway in order to enable

## TANDEM

wireless control of the motors. A proof of concept drop test experiment is currently under development. The drop test will be used to validate the modeling methodology presented in Section 8. Upon the completion of the drop tests, the landing system will be at TRL-3.

While TANDEM is a new concept with wide array of exploration options to pursue, its foundations are firmly rooted in two established technologies currently being pursued by NASA. Both tensegrity robots and semi-flexible deployable heat shields are being thoroughly investigated for their use in space exploration. Research on the ADEPT concept has thus far resulted in a high TRL 3-D woven heat shield, which can easily be adapted for TANDEM, while the up and coming field of tensegrity robotics has shown the efficiency and practicality that can be expected of highly versatile tensegrity landers. Altogether, the numerous tapped and untapped benefits presented by this concept and the foundation of research that has been instituted by the relevant literature, as well as this Phase I study, make TANDEM a low-risk/high-reward research opportunity.

### **12. Acknowledgements**

The award of the NASA Innovative Advanced Concepts (NIAC) Program Phase I grant that made the present exciting research pursuit possible is highly acknowledged and appreciated. The authors would like to personally thank each and every member of the NIAC Executive and Program Teams, NIAC Scientific Advisory Board, and the NASA Space Technology Mission Directorate at NASA Headquarters that created and supported such an important scholarly and cultural undertaking.

The authors would further like to thank the members of the NASA Ames Dynamic Tensegrity Robotics Lab, especially Vytas SunSpiral and Dawn Hustig-Schultz for their open arms to collaborate and enthusiasm for this research. Additionally, the authors wish to express their gratitude for the multifaceted contribution made to this study by the members of *CRashworthiness for Aerospace Structures and Hybrids* Laboratory (*CRASH* Lab) at Virginia Tech.

### **Appendix A: Comparison to ADEPT**

Although TANDEM and ADEPT use fundamentally the same heat shield, the full aeroshell design is very different. Because TANDEM's tensegrity structure provides the frame for the heat shield, a number of component in the ADEPT design are eliminated. Table 8 compares the mass breakdown of both TANDEM and ADEPT to highlight the differences between the two. What makes TANDEM unique is the integration of the landing and locomotion systems into the entry and descent stages of the EDLL sequence. This is where the biggest benefits can be found. The predicted mass of the mission is reduced by approximately 800 *kg* after switching from the ADEPT VITaL design to the TANDEM design. Of this mass savings, only about 100 *kg* was contributed by the decrease in heatshield diameter. The change of lander designs resulted in a predicted mass reduction of 190 *kg*. The remaining 510 *kg* in mass reduction comes directly from combining these systems together.

TANDEM

Table 8 Comparison of mass breakdown for TANDEM and ADEPT-VITaL<sup>3</sup>

Mass List	TANDEM			ADEPT-VITaL		
	CBE 1007 kg	Growth 0.3	Predicted Mass 1300 kg	CBE 1621 kg	Growth 0.3	Predicted Mass 2100 kg
<b>Aeroshell</b>	<b>338</b>		<b>432</b>	<b>807</b>		<b>1042</b>
Heat Shield	134		174	484		629
Main Body	0	0.3	0	233	0.3	303
Nose Cap & Lock Ring	61	0.3	79	61	0.3	79
Ribs & Bearings	23	0.3	30	46	0.3	60
Struts & End Fit	0	0.3	0	42	0.3	55
Joint Hardware	10	0.3	13	10	0.3	13
Carbon Cloth	40	0.3	52	92	0.3	120
Rigid Nose TPS	71		85	71		85
Nose TPS	50	0.2	60	50	0.2	60
Ribs TPS	12	0.2	14	12	0.2	14
Aft Cover TPS	9	0.2	11	9	0.2	11
Backshell	30	0.3	39	30	0.3	39
Mechanisms & Separation	86		112	205		267
Overall Deployment System	60	0.3	78	54	0.3	70
Stowed/Deployed Latched	19	0.3	25	19	0.3	25
Aeroshell Separation Ring	0	0.3	0	30	0.3	39
Separation Guild Rails	0	0.3	0	45	0.3	59
Backshell Sep	7	0.3	9	7	0.3	9
Parachute System	0	0.3	0	50	0.3	65
Avionics & Power	17		22	17		22
Avionic Unit	4	0.3	5	4	0.3	5
Harness	5	0.3	7	5	0.3	7
Power Unit	8	0.3	10	8	0.3	10
<b>Lander</b>	<b>669</b>		<b>868</b>	<b>814</b>		<b>1058</b>
Scientific Payload	37	0.3	48	37	0.3	48
Thermal	66	0.3	85	65.5	0.3	85
Power	12	0.3	16	12.3	0.3	16
Comm, Avionics, & Electronics	24	0.3	32	24.3	0.3	32
Structure	120	0.3	154	222	0.3	289
Landing System	410	0.3	533	452	0.3	588.0

**Appendix B: Comparison to VITaL**

A common design for contemporary Venus landers is the heritage design of the Venera landers<sup>25-</sup><sup>28</sup>. Venera-class landers are identified by their four distinct structural components. From top down, those four component are: the parachute capsule and drag plate, the payload module, the legs, and the impact ring. In order to show the merit of the TANDEM concept a direct comparison was made between TANDEM and a state of the art Venera-class lander for the same mission. Schroeder et al. provided a thorough design investigation of Venera-class landers, including the aforementioned ADEPT-VITaL lander<sup>3</sup>. For missions with a flat expected landing surface, it has been shown previously that the mass of a Venera-class lander can be reduced to approximately 500 kg<sup>53</sup> given the same 260 kg payload module as used in this study. For missions to the Tessera regions with heavily deformed terrain, the Venera-class lander design will approach the significantly heavier VITaL lander design. This is because additional mass is required to maintain a low center of gravity and prevent the lander from tipping over. In these uneven and steep landing environments, the tensegrity landers become more mass efficient than Venera-class landers.

*Table 9 Comparison of TANDEM to state of the art Venera-class landers*

	TANDEM	Venera-Class Baseline <sup>53</sup>	ADEPT-VITaL <sup>3</sup>	VITaL <sup>25</sup>
Payload Module**	150 kg	150 kg	149.2 kg	174 kg
Structure	110 kg	240.5 kg	212.3 kg	283 kg
Landing System	410 kg	105 kg	452.3 kg	603 kg
Total	670 kg	495.5 kg	813.8 kg	1060 kg
Terminal Velocity	23 m/s	7.87 m/s	Not Reported	9 m/s
G-Loading	96 g's	92 g's	Not Reported	83 g's

*\*\* Note: The payload module mass is comprised of scientific experiments, communications, TPS, and power. Unlike other locations in this paper, the mass of the pressure vessel is not included.*

Given that the TANDEM lander is in the same range of mass efficiency as the traditional Venera-type design, though noticeably lighter for rougher terrains, the next figure of merit to discuss is on-the-ground locomotion. The capability for locomotion expands the scientific exploration that the lander is capable of, even for short-term missions. TANDEM eliminates the risk associated with immobility while enabling the lander to fully investigate the landing site, resulting in a more complete picture of the area. It enables scientists to remotely interact with the environment and select regions of interest for focused investigation.

It is also noteworthy to compare the touchdown velocities of the two landers. The VITaL lander has a touchdown velocity of approximately 9 m/s<sup>25</sup> whereas the TANDEM vehicle impacts between 23,

## *TANDEM*

resulting in roughly the same g-load for both concepts (depending on vehicle orientation and landing surface slope). As shown in Section **Error! Reference source not found.**, the mass of the lander will decrease linearly with landing velocity. One method of decreasing the landing velocity is by keeping the backshell on during touchdown. Because the descent stage has such a low terminal velocity, it is feasible that the added back shell will not interfere with the landing sequence. The backshell can then be removed afterwards as the rover begins to roll. As the current vehicle design was driven primarily by the impact speed, if the landing speed of the rover is decreased, the vehicle mass could be reduced by 45% or more. This alternative landing sequence needs to be further analyzed and will not be discussed further in this paper.

## References

- <sup>1</sup> Schroeder, K., Bayandor, J., and Samareh, J., “Venus Lander Vehicle Concept Development Part 2: TANDEM, Tension Adjustable Network for Deploying Entry Membrane,” *Manuscript in preparation*, 2016.
- <sup>2</sup> Board, S. S., *Vision and Voyages for Planetary Science in the Decade 2013-2022*, National Academies Press, 2012.
- <sup>3</sup> Smith, B., Venkatapathy, E., Wercinski, P., Yount, B., Prabhu, D., Gage, P., Glaze, L., and Baker, C., “Venus In Situ Explorer Mission Design Using a Mechanically Deployed Aerodynamic Decelerator,” *2013 IEEE Aerospace Conference*, IEEE, 2013, pp. 1–18.
- <sup>4</sup> Venkatapathy, E., Arnold, J., Fernandez, I., Hamm, K. R., Kinney, D., Laub, B., Makino, A., McGuire, M. K., Peterson, K., and Prabhu, D., “Adaptive Deployable Entry and Placement Technology (ADEPT): A Feasibility Study for Human Missions to Mars,” *21st AIAA Aerodynamic Decelerator Systems Technology Conference and Seminar, Dublin, Ireland, AIAA Paper*, 2011.
- <sup>5</sup> Stern, E., Barnhardt, M., Venkatapathy, E., Candler, G., and Prabhu, D., “Investigation of Transonic Wake Dynamics for Mechanically Deployable Entry Systems,” *Aerospace Conference, 2012 IEEE*, IEEE, 2012, pp. 1–10.
- <sup>6</sup> Smith, B. P., Yount, B. C., Venkatapathy, E., Stern, E. C., Prabhu, D. K., and Litton, D. K., “Progress in Payload Separation Risk Mitigation for a Deployable Venus Heat Shield,” *AIAA Aerodynamic Decelerator Systems Conference, Daytona Beach, FL*, 2013.
- <sup>7</sup> Smith, B., Cassell, A., Kruger, C., Venkatapathy, E., Kazemba, C., and Simonis, K., “Nano-ADEPT: An Entry System for Secondary Payloads,” *2015 IEEE Aerospace Conference*, IEEE, 2015, pp. 1–11.
- <sup>8</sup> Warden, R. M., “Folding, Articulated, Square Truss,” 1987.
- <sup>9</sup> Belvin, W. K., Herstrom, C. L., and Edighoffer, H. H., “Quasistatic Shape Adjustment of a 15-meter-Diameter Space Antenna,” *Journal of Spacecraft and Rockets*, vol. 26, 1989, pp. 129–136.
- <sup>10</sup> Tibert, G., *Deployable Tensegrity Structures for Space Applications*, Citeseer, 2002.
- <sup>11</sup> Mirletz, B. T., Park, I.-W., Flemons, T. E., Agogino, A. K., Quinn, R. D., and SunSpiral, V., “Design and Control of Modular Spine-like Tensegrity Structures,” *The 6th World Conference of*

- the International Association for Structural Control and Monitoring (6WCSCM)*, 2014.
- <sup>12</sup> Friesen, J., Pogue, A., Bewley, T., de Oliveira, M., Skelton, R., and SunSpiral, V., “DuCTT: A tensegrity robot for exploring duct systems,” *2014 IEEE International Conference on Robotics and Automation (ICRA)*, IEEE, 2014, pp. 4222–4228.
- <sup>13</sup> SunSpiral, V., Gorospe, G., Bruce, J., Iscen, A., Korbel, G., Milam, S., Agogino, A., and Atkinson, D., “Tensegrity Based Probes for Planetary Exploration: Entry, Descent and Landing (EDL) and Surface Mobility Analysis,” *International Journal of Planetary Probes*, 2013.
- <sup>14</sup> Skelton, R. E., “Structural Systems: A Marriage of Structural Engineering and System Science,” *Journal of Structural Control*, vol. 9, 2002, pp. 113–133.
- <sup>15</sup> Chopra, S. D., Teodorescu, M., Lessard, S., Agogino, A., and SunSpiral, V., “Tensegrity Heat Shield for Atmospheric Entry Through Celestial Bodies,” *ASME 2016 International Design Engineering Technical Conferences and Computers and Information in Engineering Conference*, 2016.
- <sup>16</sup> Dutta, S., Smith, B., Prabhu, D., and Venkatapathy, E., “Mission Sizing and Trade Studies for Low Ballistic Coefficient Entry Systems to Venus,” *Aerospace Conference, 2012 IEEE*, IEEE, 2012, pp. 1–14.
- <sup>17</sup> Arnold, J. O., Peterson, K. H., Yount, B. C., Schneider, N., and Chavez-Garcia, J., “Thermal and Structural Performance of Woven Carbon Cloth for Adaptive Deployable Entry and Placement Technology,” *22nd AIAA Aerodynamic Decelerator Systems Technology Conference*, 2013, pp. 25–28.
- <sup>18</sup> Venkatapathy, E., and Ellerby, D., “Heat Shield for Extreme Entry Environment Technology for Near-Term Robotic Science Missions and Longer Term Human Missions,” *LPI Contributions*, vol. 1795, 2014, p. 8101.
- <sup>19</sup> Mitchell, D. P., “Plumbing the atmosphere of Venus,” *Mental Landscape* Available: [http://mentallandscape.com/V\\_Lavochkin1.htm](http://mentallandscape.com/V_Lavochkin1.htm).
- <sup>20</sup> Limaye, S., Smrekar, S., and Committee, V. E., “Venus White Paper for Planetary Sciences Decadal Survey Inner-Planets Panel Venus Exploration Goals, Objectives, Investigations, and Priorities,” 2009.
- <sup>21</sup> Corfield, R., *Lives of the Planets: A Natural History of the Solar System*, Basic Books, 2007.

- 22 Arnold, J. O., Laub, B., Chen, Y. K., Prabhu, D. K., Bittner, M. E., and Venkatpathy, E., “Arcjet Testing of Woven Carbon Cloth for Use on Adaptive Deployable Entry Placement Technology,” *International Planetary Probe Workshop*, 2013, pp. 17–21.
- 23 Honeybee Robotics Ltd., “Motor for High Temperature Applications,” Nov. 2013.
- 24 Keldysh, M. V., “Venus exploration with the Venera 9 and Venera 10 spacecraft,” *Icarus*, vol. 30, 1977, pp. 605–625.
- 25 Gilmore, M., and Glaze, L., “Venus Intrepid Tessera Lander,” 2010.
- 26 Hall, J. L., Bullock, M., Senske, D. A., Cutts, J. A., and Grammier, R., “Venus Flagship Mission Study, Final Report of the Venus Science and Technology Definition Team,” *Jet Propulsion Lab [online database]*, URL:[cited 15 May 1993], 2012.
- 27 Dyson, R. W., Schmitz, P. G., Penswick, L. B., and Bruder, G. A., “Long-lived Venus lander conceptual design: how to keep it cool,” *paper AIAA*, vol. 4631, 2009, pp. 2–5.
- 28 Vorontsov, V. A., Lokhmatova, M. G., Martynov, M. B., Pichkhadze, K. M., Simonov, A. V., Khartov, V. V., Zasova, L. V., Zelenyi, L. M., and Korablev, O. I., “Prospective spacecraft for venus research: Venera-D design,” *Solar System Research*, vol. 45, 2011, pp. 710–714.
- 29 Zoelly, R., “Ueber ein Knickungsproblem an der Kugelschale,” 1915.
- 30 Landis, G. A., and Harrison, R., “Batteries for Venus surface operation,” *Journal of Propulsion and Power*, vol. 26, 2010, pp. 649–654.
- 31 Hunter, G. W., Okojie, R. S., Krasowski, M. J., Beheim, G. M., Fralick, G. C., Wrbanek, J. D., Greenberg, P. S., and Xu, J., “Microsystems, Space Qualified Electronics and Mobile Sensor Platforms for Harsh Environment Applications and Planetary Exploration,” 2007.
- 32 Shampine, L. F., and Reichelt, M. W., “The Matlab ODE Suite,” *SIAM journal on scientific computing*, vol. 18, 1997, pp. 1–22.
- 33 Samareh, J. A., “A Multidisciplinary Tool for Systems Analysis of Planetary Entry, Descent, and Landing (SAPE),” 2009.
- 34 Anderson, J. D., *Hypersonic and High Temperature Gas Dynamics*, Aiaa, 2000.
- 35 Justus, C. G., and Braun, R. D., “Atmospheric Environments for Entry, Descent and Landing

- (EDL),” 2007.
- 36 Sutton, K., and Graves Jr, R. A., “A General Stagnation-point Convective Heating Equation for Arbitrary Gas Mixtures,” 1971.
- 37 Scott, C. D., Ried, R. C., Maraia, R. J., Li, C.-P., and Derry, S. M., “An AOTV Aeroheating and Thermal Protection Study,” 1984.
- 38 Tauber, M. E., Bowles, J. V, and Yang, L., “Atmospheric Environment During Maneuvering Descent from Martian Orbit,” *Journal of Spacecraft and Rockets*, vol. 26, 1989, pp. 330–337.
- 39 Park, C., and Ahn, H.-K., “Stagnation-point Heat Transfer Rates for Pioneer-Venus Probes,” *Journal of thermophysics and heat transfer*, vol. 13, 1999, pp. 33–41.
- 40 Craig, S., and Lyne, J. E., “Parametric Study of Aerocapture for Missions to Venus,” *Journal of spacecraft and rockets*, vol. 42, 2005, pp. 1035–1038.
- 41 Tauber, M. E., Palmer, G. E., and Prabhu, D. K., “Stagnation Point Radiative Heating Relations for Venus Entry,” 2012.
- 42 Tibert, A. G., and Pellegrino, S., “Review of Form-finding Methods for tensegrity Structures,” *International Journal of Space Structures*, vol. 26, 2011, pp. 241–255.
- 43 Pellegrino, S., “Mechanics of Kinematically Indeterminate Structures,” 1986.
- 44 Petropoulos, B., “Physical parameters of the atmosphere of Venus,” *Earth, Moon, and Planets*, vol. 42, 1988, pp. 29–40.
- 45 Heidaryan, E., Hatami, T., Rahimi, M., and Moghadasi, J., “Viscosity of pure carbon dioxide at supercritical region: Measurement and correlation approach,” *The Journal of Supercritical Fluids*, vol. 56, 2011, pp. 144–151.
- 46 {ANSYS Incorporated}, *Fluent 17.0 User’s Guide*, 2017.
- 47 {ANSYS Incorporated}, “ANSYS Fluent 17.0 Theory Guide,” 2017.
- 48 Rimoli, J. J., “On the impact tolerance of tensegrity-based planetary landers,” *57th AIAA/ASCE/AHS/ASC Structures, Structural Dynamics, and Materials Conference*, 2016, p. 1511.
- 49 Agogino, A., SunSpiral, V., and Atkinson, D., “Super Ball Bot-structures for planetary landing and exploration,” *NASA Innovative Advanced Concepts (NIAC) Program, Final Report*, 2013.

- <sup>50</sup> Campbell, B. A., and Campbell, D. B., “Analysis of Volcanic Surface Morphology on Venus from Comparison of Arecibo, Magellan, and Cerrestrial Airborne radar data,” *Journal of Geophysical Research: Planets*, vol. 97, 1992, pp. 16293–16314.
- <sup>51</sup> Grillner, S., “Neurobiological bases of rhythmic motor acts in vertebrates,” *Science*, vol. 228, 1985, pp. 143–150.
- <sup>52</sup> Ijspeert, A. J., Crespi, A., Ryczko, D., and Cabelguen, J.-M., “From swimming to walking with a salamander robot driven by a spinal cord model,” *science*, vol. 315, 2007, pp. 1416–1420.
- <sup>53</sup> Schroeder, K., Bayandor, J., and Samareh, J., “Venus Lander Vehicle Concept Development Part 1: Sizing and Synthesis of Venera Class Landers,” *Manuscript in preparation*, 2016.